Testing intraplate deformation in the North American plate interior from a combined geodetic solution: implication for strain accumulation on potentially seismogenic faults in the central and eastern U.S.

NEHRP Award 03HQGR0001

E. Calais
Purdue University, Department of Earth and Atmospheric Sciences
West Lafayette, Indiana 47907, USA

C. DeMets
University of Wisconsin, Department of Geology and Geophysics
Madison, Wisconsin, USA

J.M. Nocquet
CNRS, UMR6526 Géosciences Azur
Valbonne, France

Research supported by the U.S. Geological Survey (USGS), Department of the Interior, under USGS award number 03HQGR0001. The views and conclusions contained in this document are those of the authors and should not be interpreted as necessarily representing the official policies, either expressed or implied, of the U.S. Government.

Contents

Contents

Abstract

The occurrence of earthquakes in the interior of tectonic plates indicates that stresses within plate interiors accumulate on faults and are released during large, although infrequent, events. How this cycle relates to the slow deformation of plate interiors is unknown, posing significant difficulties for understanding the associated hazards. Quantifying the long-term strain associated with strain accumulation on active faults in continental interiors remains a challenge because the expected rates are close to the precision of geodetic techniques.

We present a new assessment of intraplate deformation in the North American plate interior based on data from more than 300 continuous GPS stations covering the central and eastern U.S. In order to maximize accuracy, we combined two independent geodetic solutions and derived a velocity field covering the stable interior of North America.

We find that deformation north of 40N is dominated by the effects of glacial isostatic adjustment with horizontal residual velocities to a rigid plate model up to ∼1.4 mm/yr, directed south to southeast. South of that latitude, residual velocities model show a random pattern, with a weighted misfit of 0.7 mm/yr and no evidence for regions of elevated strain rates. In particular, we find no detectable residual motion at the 95% confidence level in the New Madrid Seismic Zone, with an average weighted misfit of 0.7 mm/yr to a rigid plate model.

Assuming a simple model where characteristic earthquakes repeat regularly on a given active fault, our results imply a minimum recurrence interval of 600-1,500 years in the central and eastern U.S., consistent with earlier estimates based on the paleoseismic history assuming magnitude 7 earthquakes with 1-2 m of coseismic slip.

1 Background

Large earthquakes within stable plate interiors are direct evidence that significant amounts of elastic strain can accumulate along geologic structures far from plate boundary faults, where the vast majority of seismic energy is released. The 1811-1812 New Madrid events in the Mississippi valley are classical examples of large intraplate earthquakes (*e.g.*, Nuttli, 1983; Johnston, 1996; Hough et al., 2000; Figure 1.1), as is the 1905-1957 sequence of four M8 and greater earthquakes in Mongolia (Baljinnyam et al., 1993). Because significant intraplate earthquakes are infrequent and strain rates in continental interiors are so low, neither the rates and pattern of intraplate strain are well constrained, nor are the mechanism(s) responsible for strain accumulation and release on faults inside plates.

Prior geodetic studies have established an approximate upper bound of 2 mm/yr for residual motions across the Central and Eastern U.S. (e.g., Argus and Gordon, 1996; Dixon et al., 1996; Kogan et al., 2000; Sella et al., 2002; Marquez-Azua and DeMets, 2003). Gan and Prescott (2001) additionally reported evidence for elevated strain in the south central United States. Though slow by the standards of most plate boundary zones, deformation of 2 mm/yr nonetheless implies significant seismic hazard over a period of centuries to millenia if it represents elastic strain that accumulates over a several hundred kilometer-wide zone, such as the New Madrid seismic zone for instance Also, even though strain rates at the scale of the entire North American (NOAM) plate interior may be very small, the spatial density of reliable GPS measurements so far has not been sufficient to demonstrate that, locally, strain rates could not be significant.

We present a new assessment of intraplate deformation in the North American plate interior based on data from more than 300 continuous GPS stations covering the central and eastern U.S. and Canada, spanning the 1993-2005 period (Figure 1.1). The technical aspects of our work include two key elements: (1) the comparison and combination of independent geodetic solutions, and (2) the use of as many continuous stations as possible, with particular attention to developing realistic estimates of velocity uncertainties. An important and still unresolved issue in determining realistic uncertainties for GPS site velocities is the degree to which non-tectonic, site-specific factors such as ground contraction related to aquifer compaction, gravity-driven downslope movement, or temperature-induced monument deformation add random or systematic errors to site velocities over periods of years to decades. Analyses of site-specific noise characteristics cannot yet characterize random walk over periods longer than $\sim$5 years due to the still-short geodetic time series that are available to them (e.g. Williams et al., 2004; Beavan, 2005). Moreover, analyses of site specific noise are incapable of separating locally-derived systematic components of a site's motion from its steady tectonic motion. Lacking a strong basis for establishing accurate *a priori* estimates of site velocity uncertainties, one technique for robust detection of significant regional strain anomalies is to search for geographically coherent patterns of residual site movement with respect to the predictions of a simple undeforming plate model. We employ such a standard herein.

2 GPS Data and Processing

2.1 GPS Data

The GPS data we use are principally from the Continuously Operating Reference Station network (CORS) coordinated by the National Geodetic Survey (NGS) (Snay and Weston, 1999;

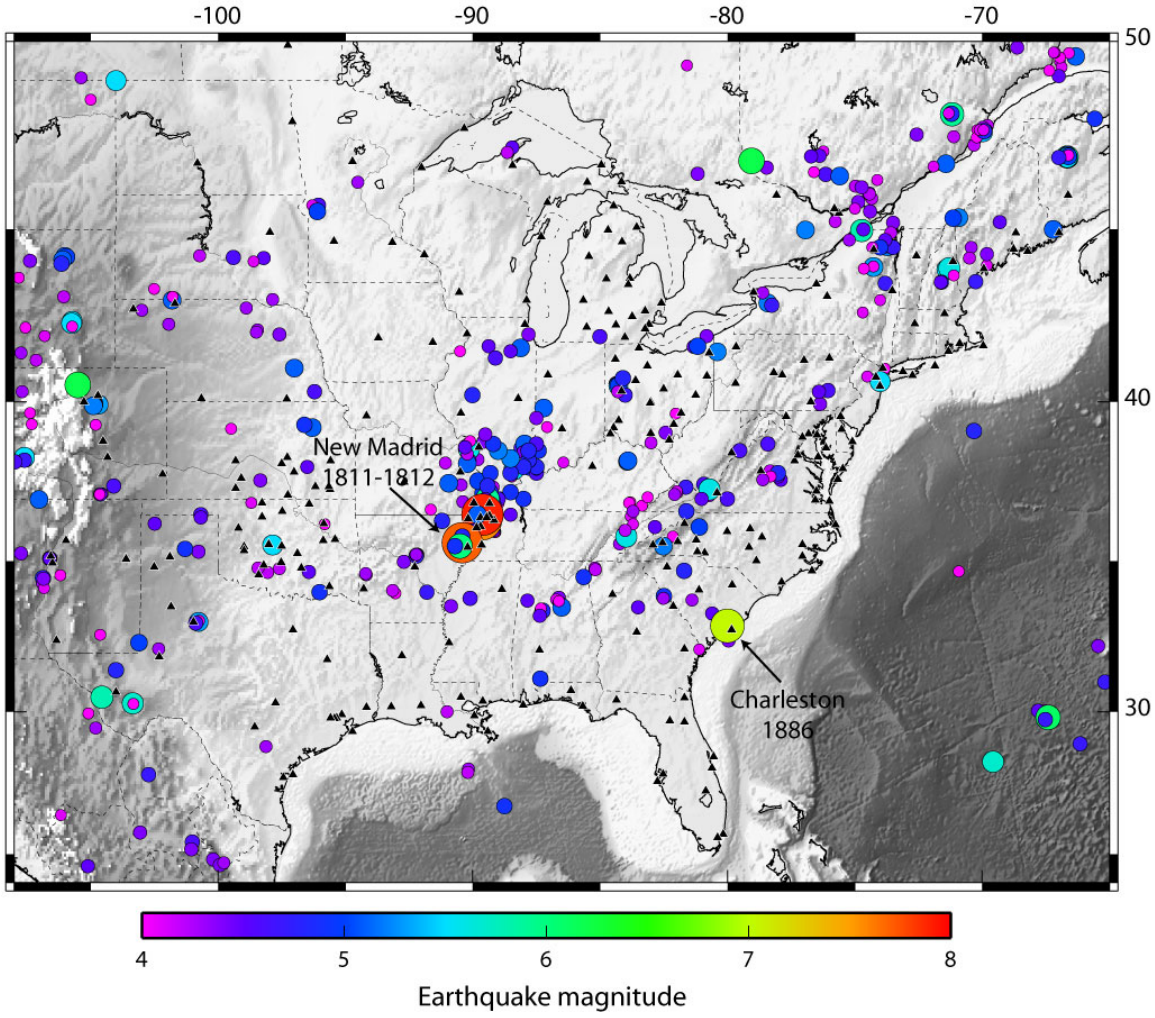

Figure 1.1: Seismicity (colored circles, M>4, NEIC catalog) and continuous GPS sites (black triangles) in the midcontinent. A number of GPS sites on this figure do not appear on Figure 3.4 because their time series is currently too short to reliably estimate a velocity.

http://www.ngs.noaa.gov/CORS/) (Figure 1.1). We also use data from a network of sites operated since 1992 by the International GPS Service for Geodynamics (IGS) and data from the GAMA network that covers the New Madrid seismic zone, operated by the Center for Earthquake Research and Information, University of Memphis (Tennessee). Numerous monument types, many of unknown stability, are employed at CORS sites, reflecting the varying requirements of the broad CORS user community. IGS site monuments are designed for precise geodynamic applications and are presumably more stable. Most GAMA sites use 60' steel H-beams (10" flange, 10" web) driven to refusal into the ground, except for MACC and CJTR, installed on the western edge of the Mississippi embayment, that use 6-9'×4"-diameter steel pipes cemented into bedrock.

2.2 Data Processing

We have processed 10 or more years of continuous data at about 450 continuous GPS sites in the central and eastern U.S. and Canada. Daily data since Jan. 1, 1993 have been processed at the University of Wisconsin using the GIPSY-OASIS software (Zumberge et al., 1997) and data since Jan. 1, 1995 have been processed at Purdue University using the GAMIT-GLOBK software (King and Bock, 2004). The GIPSY and GAMIT processing procedures we employ differ significantly and are described below.

GIPSY-OASIS processing

The GIPSY-OASIS solution is based on the precise point positioning analysis strategy described by Zumberge et al. (1997). It uses free-network satellite orbits and satellite clock offsets obtained from the NASA Jet Propulsion Laboratory (JPL). Site coordinates determined from the analysis of the GPS phase and pseudo-range observables are initially defined in a fiducial-free reference frame and subsequently transformed into the International Terrestrial Reference Frame 2000 (ITRF2000; Altamimi et al., 2002) using 7-parameter Helmert transformations that align the daily coordinates of a selected subset of ITRF2000 fiducial sites with the fiducial-free coordinates of the same subset of sites. Station velocities are calculated by a linear fit to position time series, including estimation of antenna phase center offsets where such offsets are not specified in station site logs. Uncertainties in these velocities are estimated using the Mao et al. (1999) uncertainty estimation algorithm and site-specific estimates of white, flicker, and random walk noise. Following estimation of all site velocities relative to ITRF2000, residuals for each time series are gathered and used in a time- and distance-weighted stacking algorithm to estimate and remove inter-station correlated noise. Details regarding this procedure are given by Marquez-Azua and DeMets (2003). The GIPSY velocity solution is then converted into a Solution Independent EXchange (SINEX) file that contains the estimated station positions and velocities and their complete covariance matrix for the entire time period considered (1993.0-2005+).

GAMIT-GLOBK processing

The GAMIT-GLOBK solution uses double-differenced GPS phase measurements to estimate daily station coordinates, satellite state vectors, 7 tropospheric delay parameters per site and day, horizontal tropospheric gradients, and phase ambiguities using IGS final orbits and earth orientation parameters. We apply elevation-dependent antenna phase center models following the tables recommended by the IGS, solid Earth and polar tide corrections following the IERS standards (IERS, 1996), and ocean loading corrections using the CSR4.0 ocean tide mode (Eanes, 1999) with

the 8 principal diurnal and semidiurnal tidal constituents. We then combine the (unconstrained) daily solutions from the subnetworks with global solutions produced by Scripps Institution of Oceanography into a single SINEX file for the entire time period considered (9 years).

For processing time considerations, we divided the network into regional subnetworks of about 25 sites each. All subnetworks share 6 common IGS sites (AOML, USNO, ALGO, NLIB, MDO1, AMC2) well determined in ITRF2000. These sites serve to tie the subnetworks together and with the ITRF.

Other solutions used

In addition to the GAMIT and GIPSY solutions described above, we use the global solutions provided by the IGS, which results from the combination of individual solutions from IGS analysis centers and goes back to February 1999. This solution however only include a few sites in the central and eastern US.

Finally, we use the full definition (i.e., estimates and complete covariance matrix) of the ITRF2000 (Altamimi et al., 2002). The ITRF2000 is the current realization of the International Terrestrial Reference System (ITRS) published by the International Earth Rotation Service (IERS). Using the ITRF2000 in the combination of permanent GPS solutions ensures the consistency of the resulting solutions at a continental scale. For instance, Altamimi et al. (2002) show that global-scale GPS solutions are not consistent among themselves in the definition of the scale factor and the center of mass of the Earth. This may have a significant impact on continental-scale GPS-derived velocities, in particular for the vertical component. The ITRF2000, on the other hand, includes 3 VLBI and 7 SLR solutions in order to ensure the best definition of the scale factor and the Earth's center of mass, as well as their time derivatives. Consequently, using the ITRF2000 solution as a backbone for the combination of individual GPS solutions will ensure the origin and scale stability of our combined solution. Finally, the ITRF2000 includes a NOAA solution for the CORS GPS network, with data until 2000.

2.3 Combination Procedure

A key aspect of our work is the geodetic combination of independent geodetic site coordinate and velocity solutions. Rigorous combination of alternative geodetic solutions offers a number of important advantages over using a single velocity solution, including averaging down of random and any systematic errors associated with individual processing strategies, outlier detection via cross-checking of the independent solutions, and definition of a single consistent reference frame for the combined solutions. An important additional outcome of the quality checks is a set of realistic estimates for the velocity uncertainties.

We use the combination algorithm developed by Altamimi et al. (2002), also used to calculate ITRF2000, starting with minimally constrained geodetic solutions. The combination consists of simultaneously estimating, for each site i in solution s (s = GAMIT, GIPSY, IGS, ITRF2000), the velocity $\dot{X}^i_{comb}$, and a 14-parameter transformation between the individual and the combined solution using:

$$
\begin{aligned}
X_s^i &= X_{comb}^i + (t_s - t_0)\dot{X}_{comb}^i \\
&+ T_k + D_k X_{comb}^i + R_k X_{comb}^i \\
&+ (t_s - t_k)[\dot{T}_k + \dot{D}_k X_{comb}^i + \dot{R}_k X_{comb}^i]
\end{aligned} \tag{2.1}
$$

$$
\dot{X}_s^i = \dot{X}_{comb}^i + \dot{T}_k + \dot{D}_k X_{comb}^i + \dot{R}_k X_{comb}^i \tag{2.2}
$$

where:

- X_s^i is the position of site i in solution s at epoch t_s, X_{comb}^i the estimated position of site i at epoch t_0, and $\dot{X}_{comb}^i$ its final velocity in the combination.
- T_k, D_k, R_k and $\dot{T}_k, \dot{D}_k, \dot{R}_k$ are the transformation parameters between individual solutions s and the combined solution and their time derivatives.
- t_s is the epoch of minimal position variance for the solution s, which is generally the middle point of the observation time span included in the solution.
- t_k is the epoch of expression of the transformation parameters.

The reference frame definition in the combination is implemented by imposing the 14-parameter transformation between ITRF2000 and the combined solution to be zero (no translation, scale factor, or rotation and no rate of change of these parameters). The resulting velocity field is therefore expressed in ITRF2000.

From the preliminary combination, an a posteriori variance factor σ_s^2 is estimated for each individual solution s in the inversion, at the same time as the other parameters. This variance factor is then applied to the covariance matrix of the corresponding individual solution in an iterative way until both individual σ_s^2 and the global a posteriori variance factor equal unity. As a result of this iterative scaling, formal errors of the combined solution depend on the variance of the individual solutions before the combination, but also on the level of agreement between solutions in the combination.

2.4 Statistics of the Combination

The result of the combination is a SINEX file in which positions and velocities are expressed in the ITRF2000. Table 2.1 gives the statistics of the combination. We obtain variance scaling factors ranging from 1.4 to 5.6, consistent with empirical scaling factors derived from time series analysis (Zhang et al., 1997, Mao et al., 1999, Williams, 2003). The GIPSY solution has a lower variance factor because velocity uncertainties were estimated with a model that includes white, flicker, and random walk noise. The χ^2 is very close to 1 for each of the 4 individual solutions in the combination, meaning that the 14-parameter transformation model used in the combination procedure is consistent with the uncertainties of the individual solutions and with their residuals in the combination (given the scaling factors shown in Table 2.1).

The resulting velocity field describes surface motions at 315 sites in the central and eastern U.S. and Canada, 160 of which have time series longer than 3 years. The best determined sites ($\sim$10 years of data) have respective horizontal and vertical standard deviations of $\pm$0.4 mm/yr and $\pm$0.6 mm/yr.

solution	a posteriori variance factor	Position WRMS in mm horizontal	vertical	Velocity WRMS in mm/yr horizontal	vertical
ITRF	3.1	0.7	3.8	0.4	0.6
IGS	11.9	2.3	6.3	0.6	1.0
GIPSY	0.8	2.0	1.5	0.3	0.5
GAMIT	7.4	1.1	4.0	0.5	1.9

Table 2.1: Statistics of the combination.

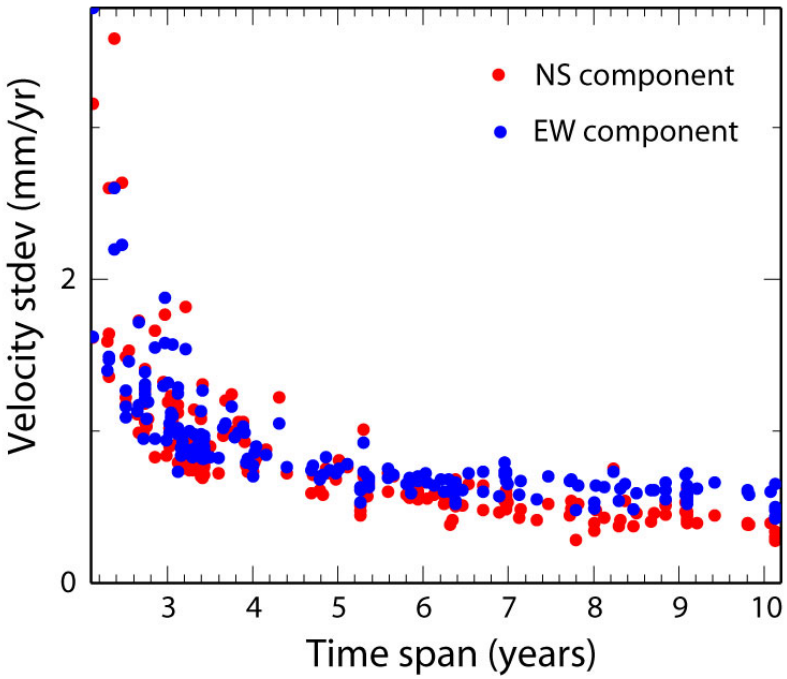

Figure 2.1: Velocity standard deviation as a function of measurement time span.

We find that velocity uncertainties decrease steadily with time for both components, slightly faster for the NS component, with the most significant improvement after 3 years of continuous measurements (Figure 2.1). This is consistent with predictions by Blewitt and Lavallee (2002), who show that at least 2.5 years of measurements are required to average out the effects of unmodeled seasonal processes such as hydrological or atmospheric loading, tropospheric heterogeneities, etc.

2.5 GAMIT-GIPSY comparison

One useful outcome of our analysis is a comparison of the individual GAMIT and GIPSY solutions for a large number of sites and over a long time period. Applying procedures outlined in the preceding section, we estimated and applied a 14-parameter Helmert transformation between the individual GIPSY and GAMIT solutions and the IGS combined solution using 28 common IGS sites. We then subtracted the North America-ITRF2000 rigid rotation described below from the resulting GAMIT and GIPSY velocity fields and compared residual velocities at the 211 common sites between the two solutions (Figure 2.2). The horizontal components of the GAMIT and GIPSY site velocities agree within 0.6-0.8 mm/yr on average, with a negligible bias (0.08 and

-0.04 mm/yr for the EW and NS components, respectively). Differences in the vertical component are larger, typically within 3 mm/yr of their mean value.

Figure 2.3 shows the 3-D coordinate time series for site MD01 in Texas reduced by the long-term North American plate motion. Daily coordinate repeatabilities for the GIPSY-derived time series are 1.6 mm in north, 3.1 mm in east, and 6.6 mm in vertical, 25-50% smaller than reported by the Scripps Orbit and Permanent Array Center (sopac.ucsd.edu) and the Jet Propulsion Laboratory (sideshow.jpl.nasa.gov/mbh/series.html) for this site. Noise over periods longer than one day is similarly smaller than that reported by SOPAC and JPL, but is similar in phase. All of the reduction in the daily and longer-period noise is attributable to the post-processing algorithm that we use for common-mode error estimation and correction.

The coordinate time series for site MDO1 (Figure 2.3) from the GAMIT analysis is surprisingly different from that from the GIPSY analysis. Daily noise in the GIPSY-derived time series is 25-50% smaller than from the GAMIT analysis and significant differences exist in the character of longer period noise (compare for example the difference in long period noise in the east component from 2002.0-2003.0). Most of these differences are likely to arise from the differing analysis strategies used for the GAMIT and GIPSY processing described above, including the use of undifferenced (GIPSY) versus double-differenced (GAMIT) GPS observables, point-positioning (GIPSY) versus regional network (GAMIT) approach. and correction of the GIPSY-derived time series for inter-site correlated noise.

3 Analysis of the velocity field

3.1 Defining rigid North America

Efforts to detect and model strain anomalies in the North American plate interior that are caused by tectonic processes, post-glacial isostatic rebound, or possibly groundwater withdrawal, require a well-defined North American plate reference frame. One end-member approach for defining such a reference frame is to exclude *a priori* all sites in predefined geographic areas where deformation could occur. For example, excluding all sites located north of 40N should reduce possible effects of glacial isostatic adjustment (GIA) that may affect the entire North America continent at a level detectable with sufficiently accurate CGPS measurements (*e.g.*, Peltier, 1998). Similarly, eliminating sites west of 110W should eliminate any effect of deformation west of the Rio Grande rift and central Colorado.

We tested for the impact of GIA effect on horizontal velocities by dividing GPS site into two subnetworks, separated by the neutral line of null vertical motion ("hinge line") that also marks a sharp decrease in horizontal motions in GIA models. Although the rheological parameters and ice history that drive GIA are still debated, most GIA models place the hinge line between 40N and 45N. We therefore estimate a single angular velocity for the entire data set (east of 110W) and compare it to the joint estimation of two angular velocities for two subnetworks including sites north or south of 40N. We use an F-test to determine whether the improvement in fit in a model with two subnetworks exceeds that expected solely from adding three model parameters. The more complex two-subnetwork model improves the fit at the 99% confidence level, thereby confirming that horizontal velocities north of 40N differ significantly from those farther south. The effect of post-glacial isostatic adjustment is the most plausible interpretation for this difference (see discussion below).

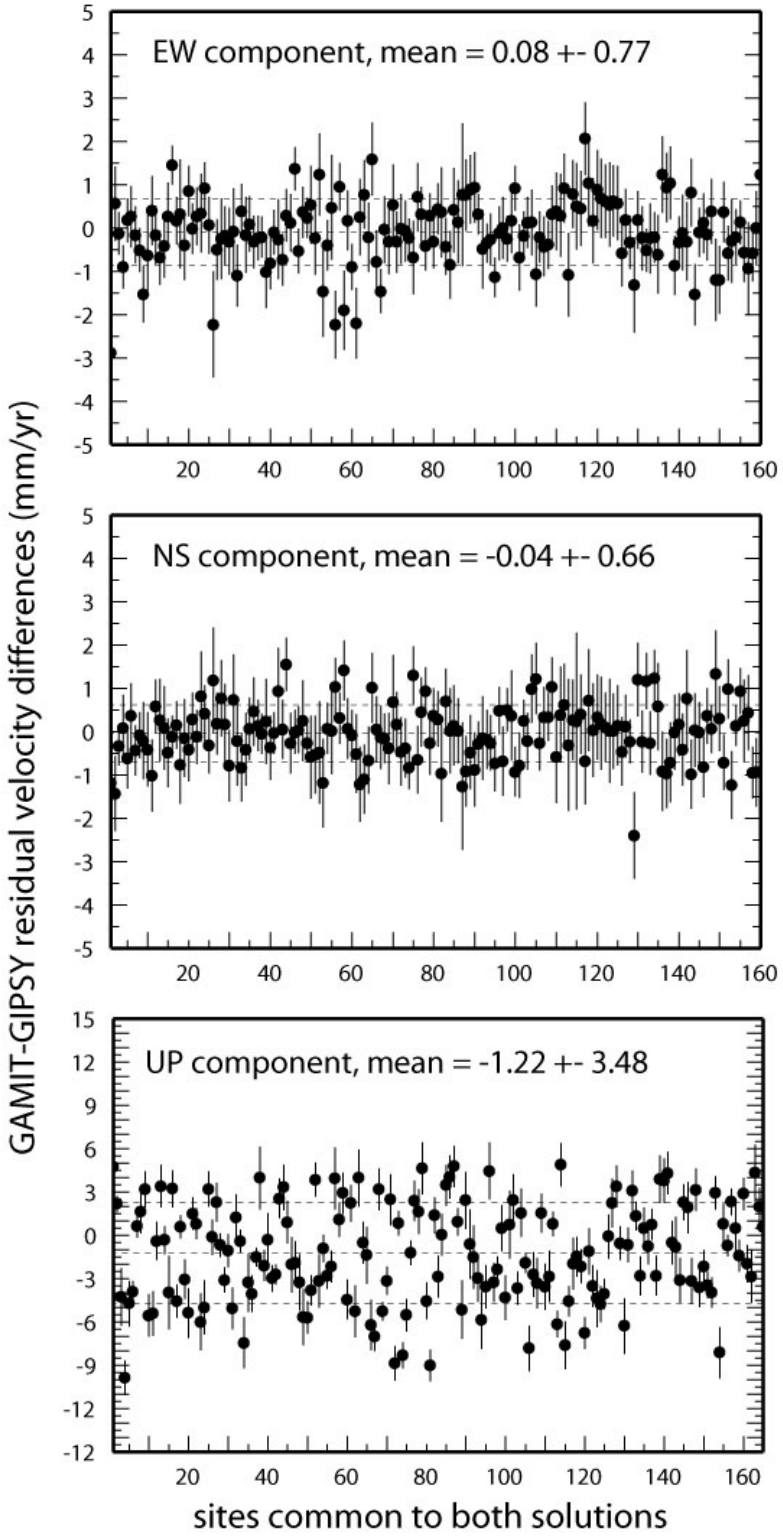

Figure 2.2: Comparison between the Gamit and Gipsy solutions. Dots show the difference, site by site, between the Gamit and Gipsy velocity estimates.

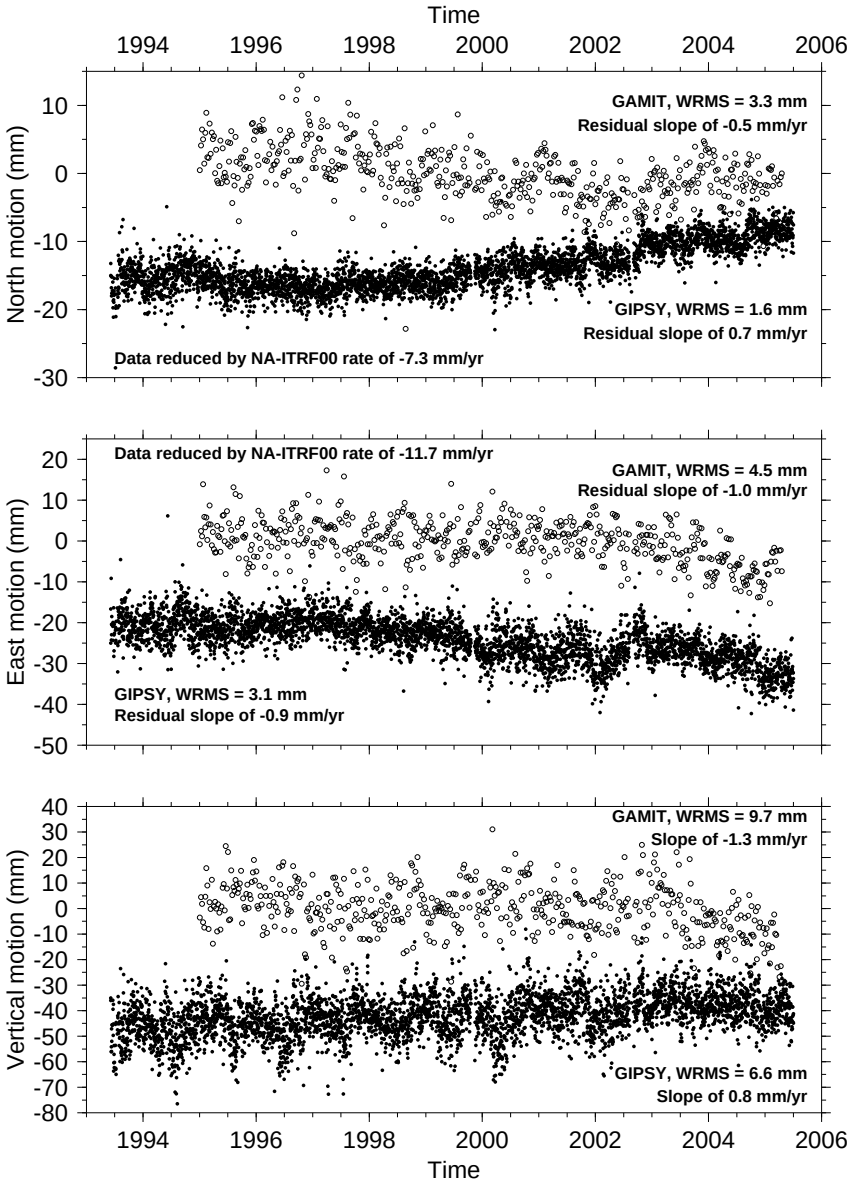

Figure 2.3: Coordinate time series for site MDO1 in Texas from GIPSY (solid circle) and GAMIT (open circle) analysis. Site motion is reduced by the North American plate motion predicted by the best-fitting North America-ITRF2000 angular velocity reported below. Abbreviation: WRMS represents the weighted root-mean-square daily residual with respect to the long-term site motion.

Based on the above results, we calculate the North American plate angular velocity with respect to ITRF2000 using sites located east of 110W and south of 40N. Using all the available sites leads to a reduced χ^2 of 1.03, with a WRMS of 0.98 mm/yr (Figure 3.1). Our best-fitting NOAM/ITRF2000 angular velocity (lat = -3.12 $\pm$ 1.11 degrees, lon = -84.74 $\pm$ 0.25 degrees, ang = 0.199 $\pm$ 0.003 deg./Ma; Figure 3.2) is very close to recent values from Beavan et al. (2002), Fernandes et al. (2003), Altamimi et al. (2002), and Marquez-Azua and DeMets (2003). Residual velocities are given in the Appendix (Table 6.1).

If we invert site velocities with successively smaller standard errors (reflecting sites with longer and thus presumably better determined velocities), the resulting best-fitting angular velocities do not change significantly and the predictions of those alternative angular velocities differ by less than 0.2 mm/yr in the plate interior (Figure 3.1). All of the data, including those with the shortest time series and hence largest uncertainties, are thus consistent with our best-fitting angular velocity. For the 133 sites with the best determined velocities, corresponding to those with velocity standard deviations smaller than 1 mm/yr, the WRMS of the residual velocities is 0.65 mm/yr.

We then examined more closely the distribution of residual velocities after removing the best-fitting NOAM/ITRF angular velocity found above. Figure 3.3A shows that residual velocities follow a Gaussian distribution about a zero-mean at sites located south of 40N. Sites located north of 40N, on the other hand, shows a deviation from a zero-mean, both on the NS and EW components (Figure 3.3B). The same observation holds for the best monumented sites (category A sites, see discussion below; Figure 3.3C and D). This deviation of velocity residuals from a zero-mean north of 40N is consistent with the F-test described above and most likely results from the effect of GIA on horizontal motions.

Residual velocities are shown in map view on Figure 3.4. The pattern of residual velocities appears random south of 40N, whereas a systematic pattern seems to emerge north of that longitude, in particular in the northeastern U.S. Note that residual velocities are not significant at most sites at the 95% confidence level. In the following, we explore residual velocities further with a particular attention to monument quality.

3.2 Monument stability

For the 211 GPS sites that are located within what we nominally define as the undeforming North American plate interior, the dispersion of the residual velocities can be used to address the possible interdependence – or lack thereof – between velocity reliability and both monument quality or observation time span.

Monument quality and stability is a significant issue in the study area because most of the CGPS installations were not primarily designed for tectonic applications. A variety of setups are in use, from concrete pillars to rooftops. NGS recently collected information on monument setup at all the CORS sites (G. Sella, pers. comm.). On that basis, we divided the sites in two categories. The A-category contains the best setups for tectonic applications, with the monument installed in the ground and either braced, or an anchored pillar, or a metal rod driven to refusal. The B-category contains rooftop monuments and ground monuments that do not belong to the categories above, such as fence posts, unbraced monuments, masts, towers, etc.

In order to quantify site quality independently from direct observations of the monuments, we

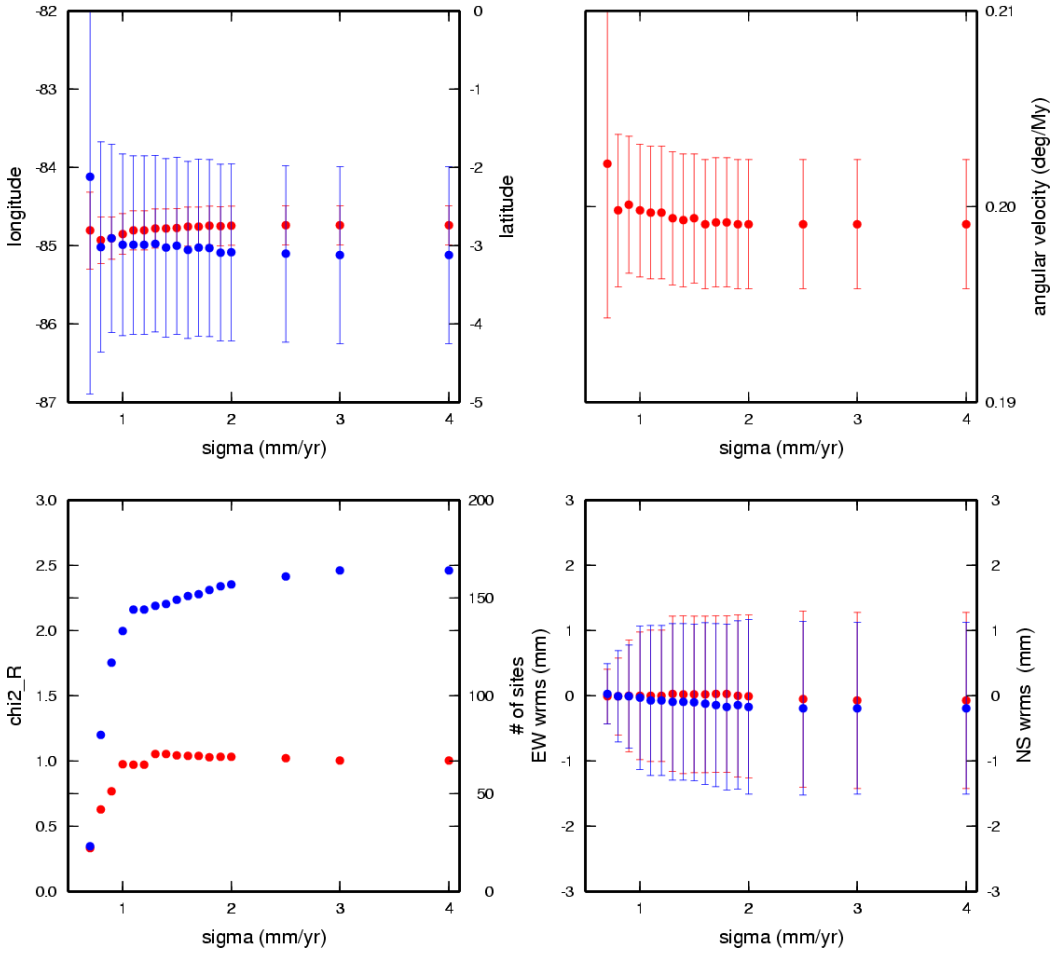

Figure 3.1: NOAM/ITRF angular velocity as a function of site selection. Each estimation is based on sites with a velocity standard deviation less than "sigma". A. Latitude (blue) and longitude (red) of Euler pole; B. Angular rate; C. χ^2 (red) and number of sites (blue); D. Distribution of residual velocities at the sites used in the estimation. Circles shows mean, error bar shows one standard deviation. EW component (red) and NS component (blue).

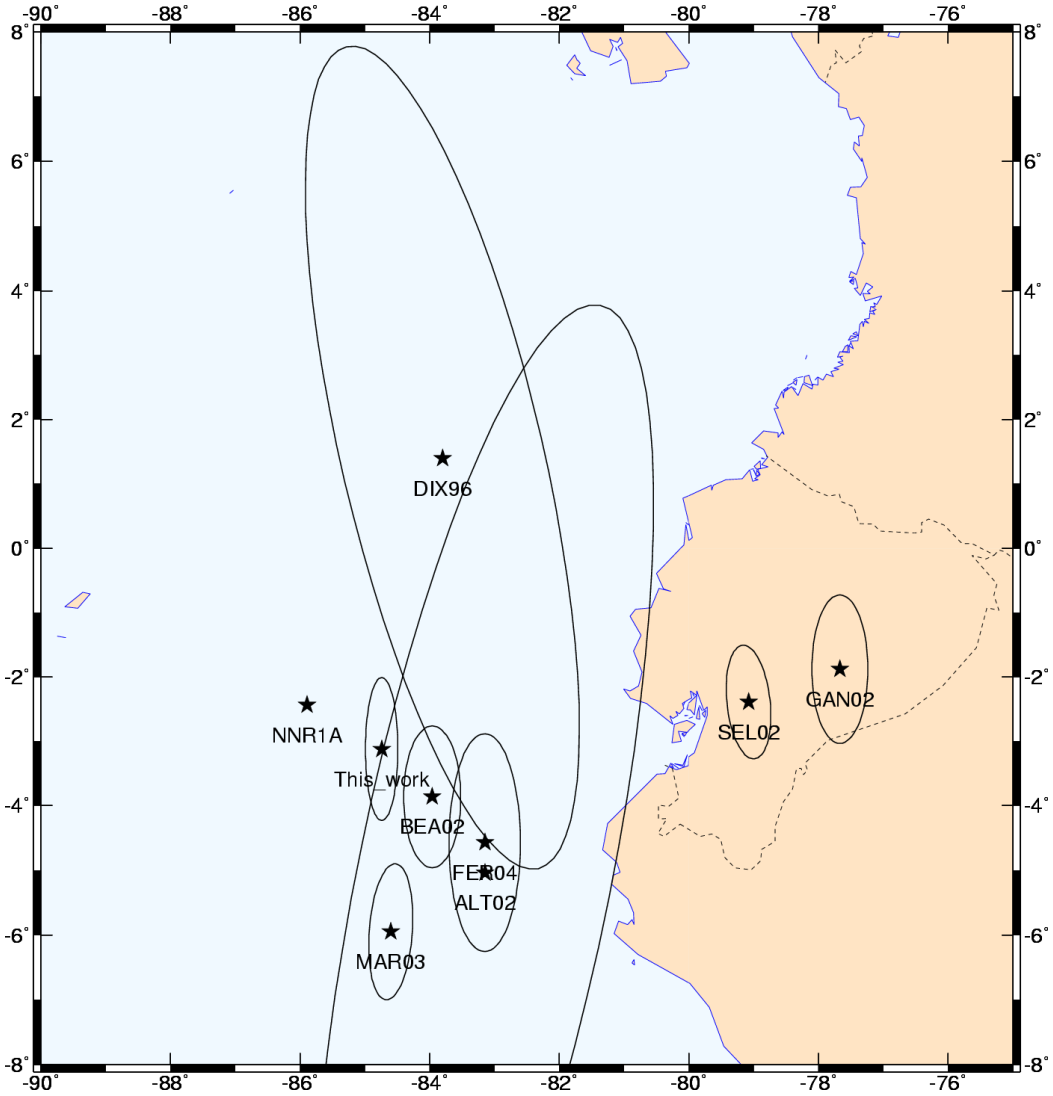

Figure 3.2: Location of the North America / ITRF rotation pole (ALT02: Altamimi et al., 2002; NNR1A: DeMets et al., 1994; SEL02: Sella et al., 2002; DIX96: Dixon et al., 1996; GAN02: Gan and Prescott, 2002, MAR02: Marquez-Azua and DeMets, 2003; BEA02: Beavan et al., 2002; FER04: Fernandes et al., 2004).

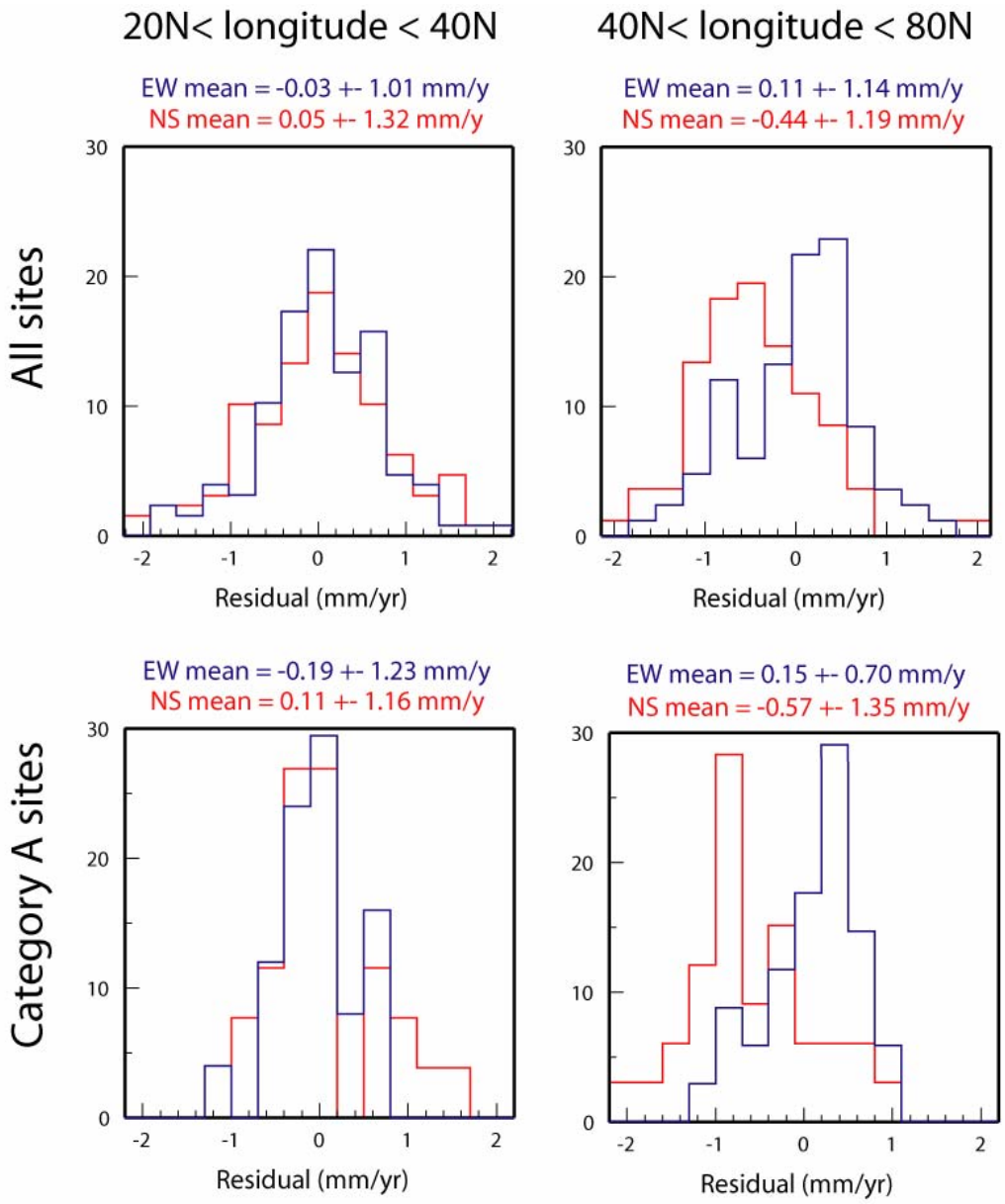

Figure 3.3: Distribution of residual velocities. A. All sites south of 40N; B. All sites north of 40N; C. Category A sites south of 40N; D. Category A sites north of 40N.

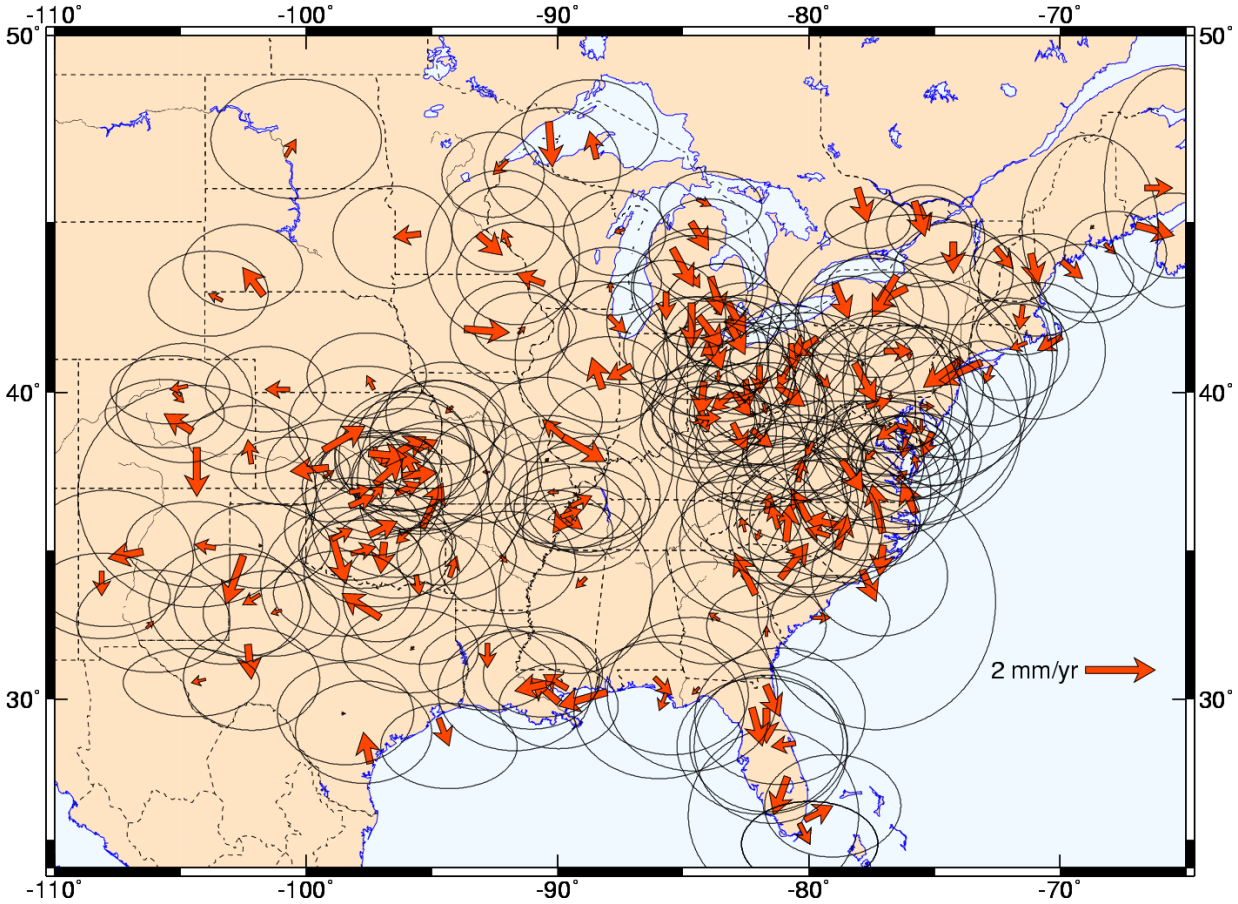

Figure 3.4: Residual velocities in the central and eastern U.S. after removal of the best-fit NOAM/ITRF angular velocity. Only sites with velocity standard deviation less than 2 mm/yr and velocity magnitude less than 1.5 mm/yr are shown here. Ellipses are 95% confidence.

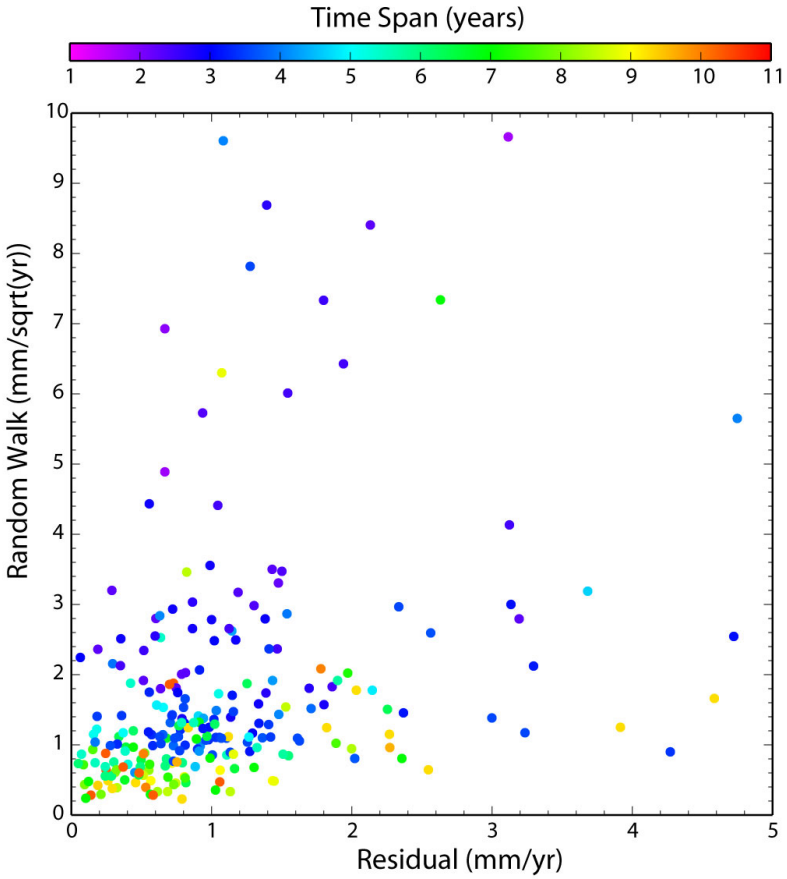

Figure 3.5: Residual velocities as a function of random walk noise.

computed the magnitude of a random-walk noise component from position time series (Langbein and Johnson, 1997). We find RWN magnitudes at most sites in the 0-2 mm/sqrt(yr) range, but reaching up to 10 mm/sqrt(yr) overall. Sites with observation time span greater than 5 years show a positive correlation between RWN magnitude and residual velocity (Figure 3.5), indicating that monuments of poorer quality tend to lead to larger residual velocities. Sites with observation time span shorter than 5 years typically show significantly larger RWN magnitude, which may reflect a limitation in the RWN estimation process, since a minimum of 5 years of continuous observations is necessary to reliably estimate RWN parameters (Langbein and Johnson, 1997).

Finally, the distribution of sites as a function of RWN (Figure 3.6) shows that the percentage of category A sites with small (< 1.5 mm/yr) residual velocities is significantly larger that for category B sites. This shows, again, a correlation between monument quality and residual velocities.

If the NOAM plate was perfectly rigid and monument quality was perfect, then residuals should decrease as the observation time span increases (*i.e.*, as velocity uncertainties decrease, since the two are correlated). We actually find that residual magnitudes decrease very slowly, if at all, after about 3.5 years of observations (Figure 3.7). Similarly, velocity uncertainties and residuals are poorly correlated (Figure 3.8). In particular, large residuals (> 2 mm/yr) are found at sites with small velocity uncertainties and long observation span. This is not true, however, for the best-quality sites (RWN < 1 mm/$\sqrt{yr}$ and category A sites), that show significantly smaller

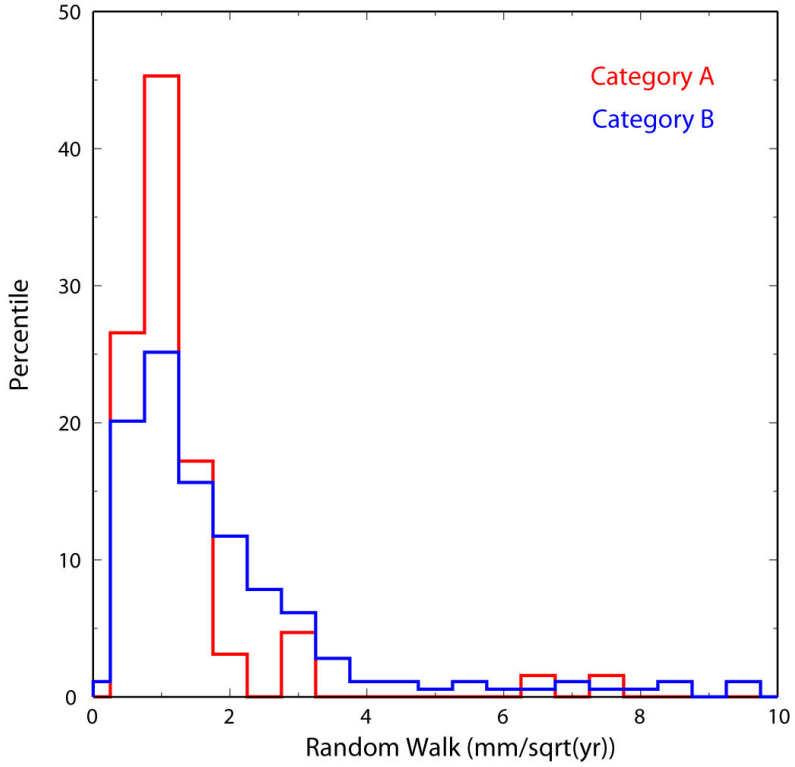

Figure 3.6: Site distribution as a function of RWN magnitude for category A (red) and B (blue) sites.

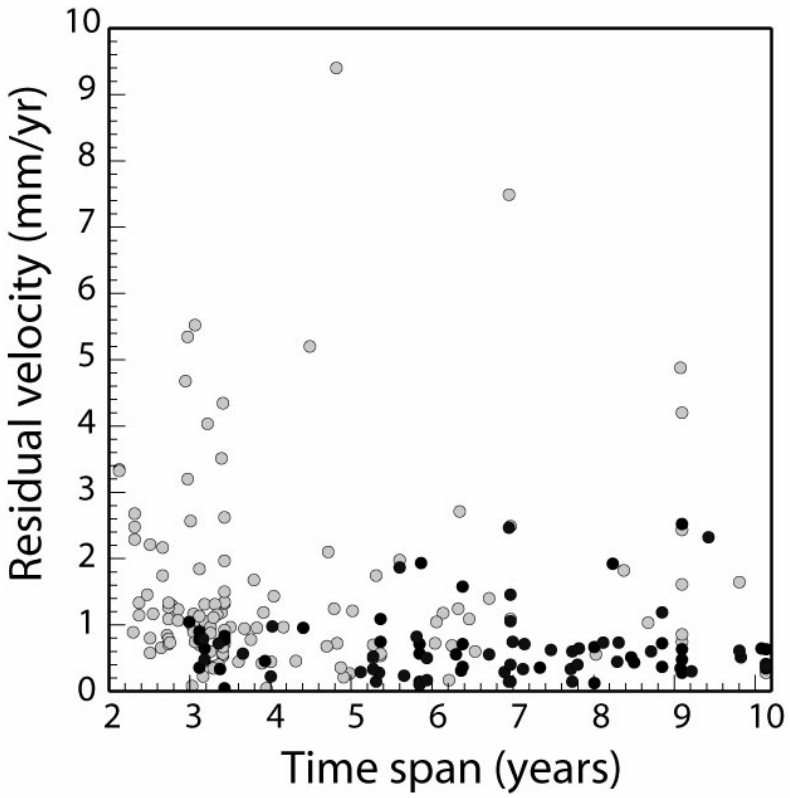

Figure 3.7: Residual velocities as a function of observation time span. Black circles are sites with RWN magnitude < 1 mm$\sqrt{yr}$ and category A sites.

velocity residuals and standard deviation than other sites, on average. We will see below that the best-quality sites with residual velocities larger than ∼1 mm/yr correspond to sites located north of 40N and likely to be affected by GIA effects. For the remaining sites, the lack of correlation between residual velocity and their uncertainty is likely to reflect their poor monumentation quality (or local effects driven by hydrological conditions). This is supported by the correlation between monument quality and residual velocities mentioned above. This results points to an intrinsic limitation to determine even smaller bounds on plate rigidity based on the entire set of CGPS sites available in the North American plate interior. Only the best-quality sites, on the basis of the stability of their monumentation and the linearity of their position time series, should be used for monitoring intraplate deformation.

4 Discussion

4.1 Glacial Isostatic Adjustment

GIA affects most of the North American continent, with a maximum predicted present-day uplift rate of ∼15 mm/yr centered on Hudson Bay, decaying radially with distance. The effect of GIA on horizontal deformation on North America is also significant, with a predicted NS gradient up to 2 mm/yr between Hudson Bay and the Gulf of Mexico. Predictions of surface deformations caused by GIA differ significantly depending on the combinations of Earth models and space

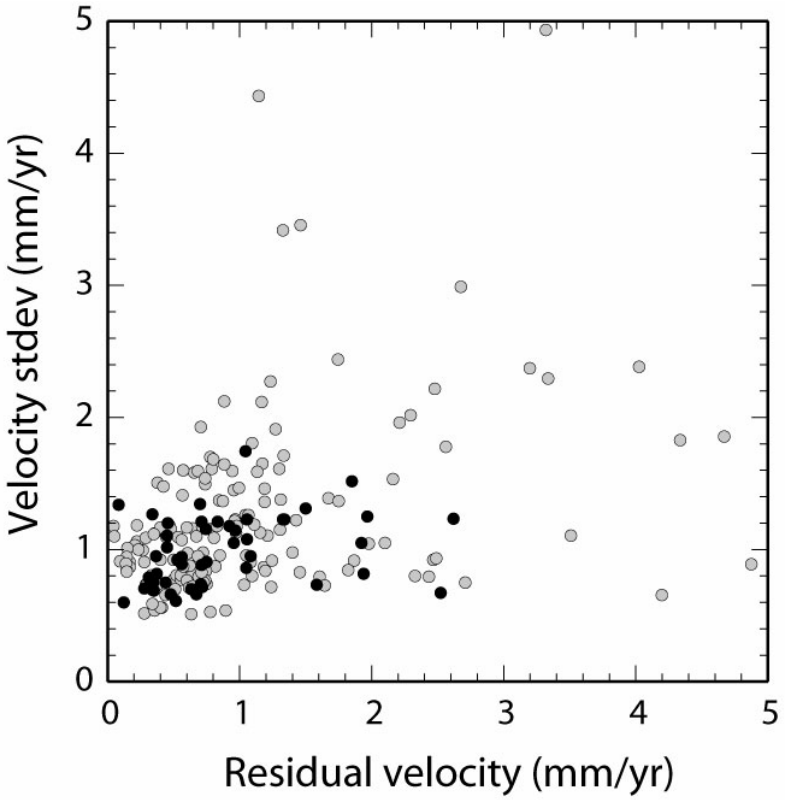

Figure 3.8: Residual velocities as a function of velocity standard deviation. Black circles are sites with RWN magnitude < 1 mm$\sqrt{yr}$ and category A sites.

and time deglaciation history. Hence, surface measurements of 3-dimensional deformations at a continental scale have the potential to discriminate between models, providing in particular better constraints on mantle viscosity. Peltier (1998) showed that the NS gradient of horizontal velocities across North America due to GIA is at least double in model VM2 than in VM1, whereas vertical velocities differ insignificantly. Hence, horizontal velocities may have more discriminating power than vertical for mantle viscosity.

In North America, few studies have yet compared modern space geodetic measurements with GIA models. Argus et al. (1999) used very long baseline interferometry and satellite laser ranging measurements and showed that the early VM1 model of Peltier (1994) fits their data better than the subsequent version VM2 (Peltier, 1996). However, their conclusion rests on less than 10 measurement sites. Park et al. (2002) compared vertical velocities at 60 continuous GPS stations in the northeastern U.S. with GIA models and found best-fit viscosities of 2×10^{20} Pa.s and 4.1 to 5.4×10^{21} Pa.s for the upper and lower mantle, respectively, independently of the lithospheric thickness. Their results are however based on a limited number of sites covering a small area and only consider vertical displacements.

Our vertical site motions (Figure 4.1) shows a clear GIA pattern with uplift rates up to 11 mm/yr around Hudson Bay decreasing southward to zero at the latitude of the Great Lakes. The hinge line is located around 40N. Vertical motion over most of the central and eastern U.S. is close to zero or shows slight subsidence.

As described above, the distribution of horizontal residual velocities also appears to be affected by GIA effects. Figure 4.2 shows residual velocities in the stable interior of North America (*i.e.*, including Canada), with uncertainty ellipses omitted for a sake of clarity. Velocities south of 40N show a random pattern, as noted above, but sites north of that longitude define a more coherent pattern, with residual velocities pointing south to southeast-ward. This is particularly visible at sites CHUR, FLIN, and DUBO in Canada, as well as at sites in the Great Lakes area, upper Midwest and New England. Using only the best-determined sites (RWN component $<$ 1 mm/$\sqrt{yr}$, see discussion above), we find a WRMS of residual velocities of 0.7 mm/yr and 1.4 mm/yr for sites located south and north of 40N, respectively. These results confirm that only sites located south of 40N should be used to define a stable North America reference frame. In addition, the lack of a systematic velocity pattern south of 40N appears to match predictions of model VM1 better than VM2 (Peltier, 1998).

4.2 The New Madrid Seismic Zone

Although our residual velocity field for the central and eastern U.S. south of 40N shows no obvious pattern of regional-scale strain, the existence of regions of significant localized strain in the central and eastern U.S. has been suggested by several authors. For instance, using a GPS-triangulation comparison, Liu et al. (1992) found a shear strain rate of 0.108±0.045 μrad/yr in the southern part of the NMSZ, corresponding to a slip rate of 5 to 7 mm/yr of slip rate. Snay et al. (1994), however, using similar data in the northern part of the NMSZ, found strain rates of 0.030±0.019 μrad/yr, indistinguishable from zero. Similarly, Weber et al. (1998) and Newman et al. (1999), using GPS data from campaigns performed between 1991 and 1997, found a slip rate of 0.2±2.4 mm/yr in the NMSZ. Gan and Prescott (2001) analyzed GPS data from continuous GPS stations in the central and eastern U.S. and argue for significant deviations from rigid plate behavior in the Mississippi embayment, which they interpret as evidence for elevated strain rates.

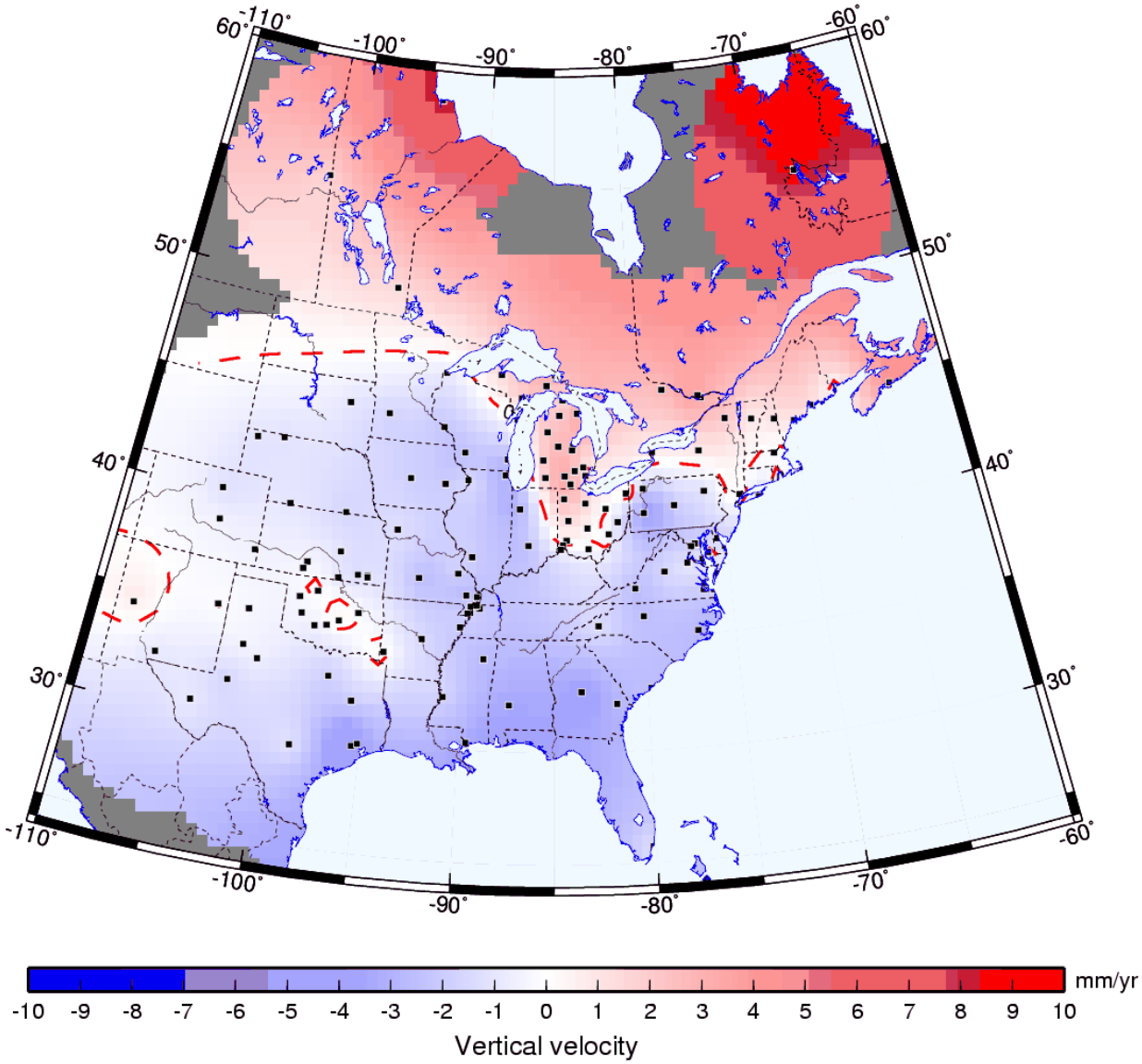

Figure 4.1: Interpolated vertical velocities. Only sites with RWN magnitude < 1 mm/$\sqrt{yr}$, category A sites, and sites with velocity standard deviation less than 1.5 mm/yr are used. Black squares show the site locations. The red dashed line correspond to zero velocity. The interpolation scheme uses an adjustable tension continuous curvature surface gridding algorithm with a tension factor of 0.9.

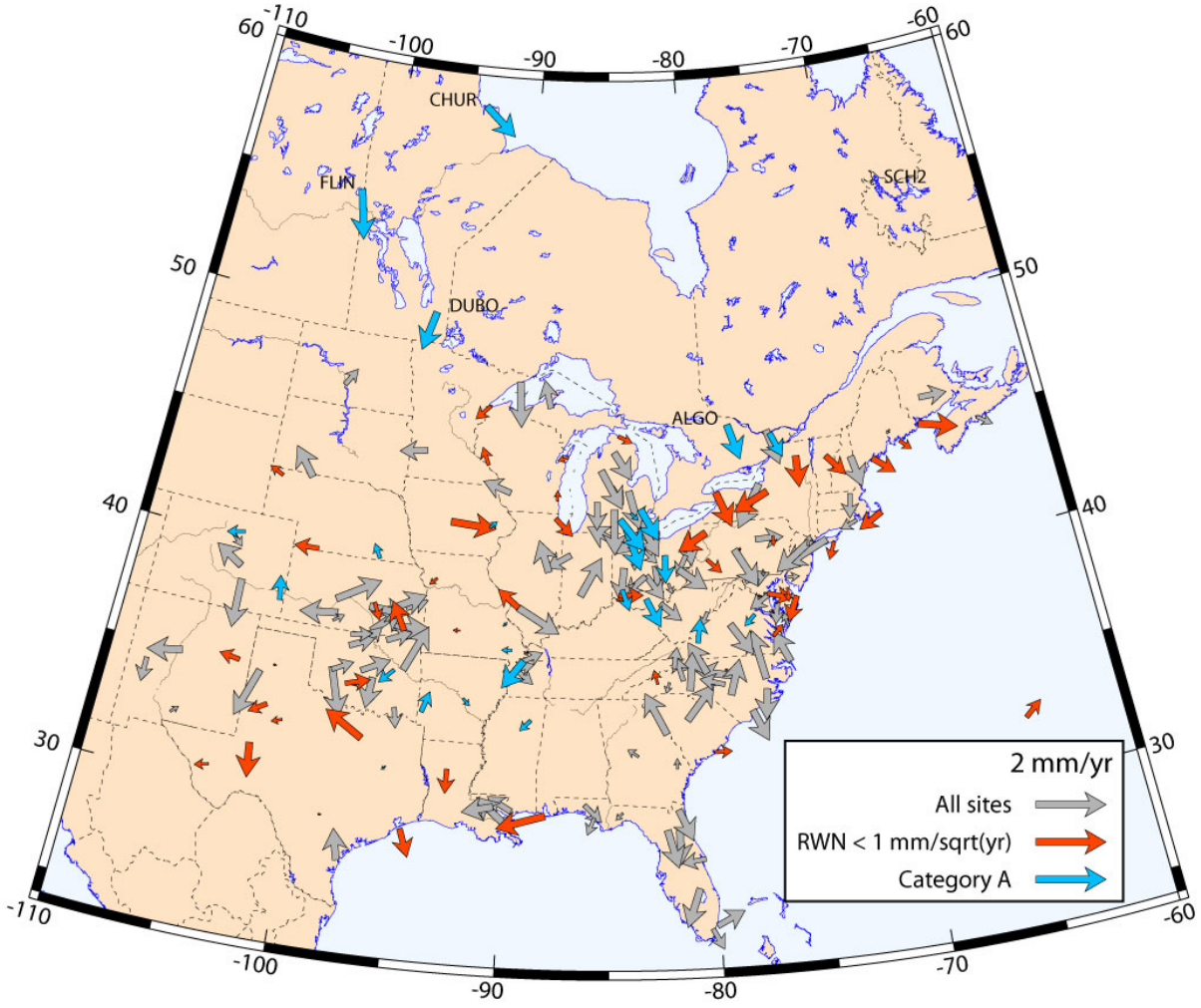

Figure 4.2: Residual velocities with uncertainty ellipses omitted for a sake of clarity. Sites with RWN magnitude < 1 mm/$\sqrt{yr}$ are shown in red, category A sites in blue, other sites in grey.

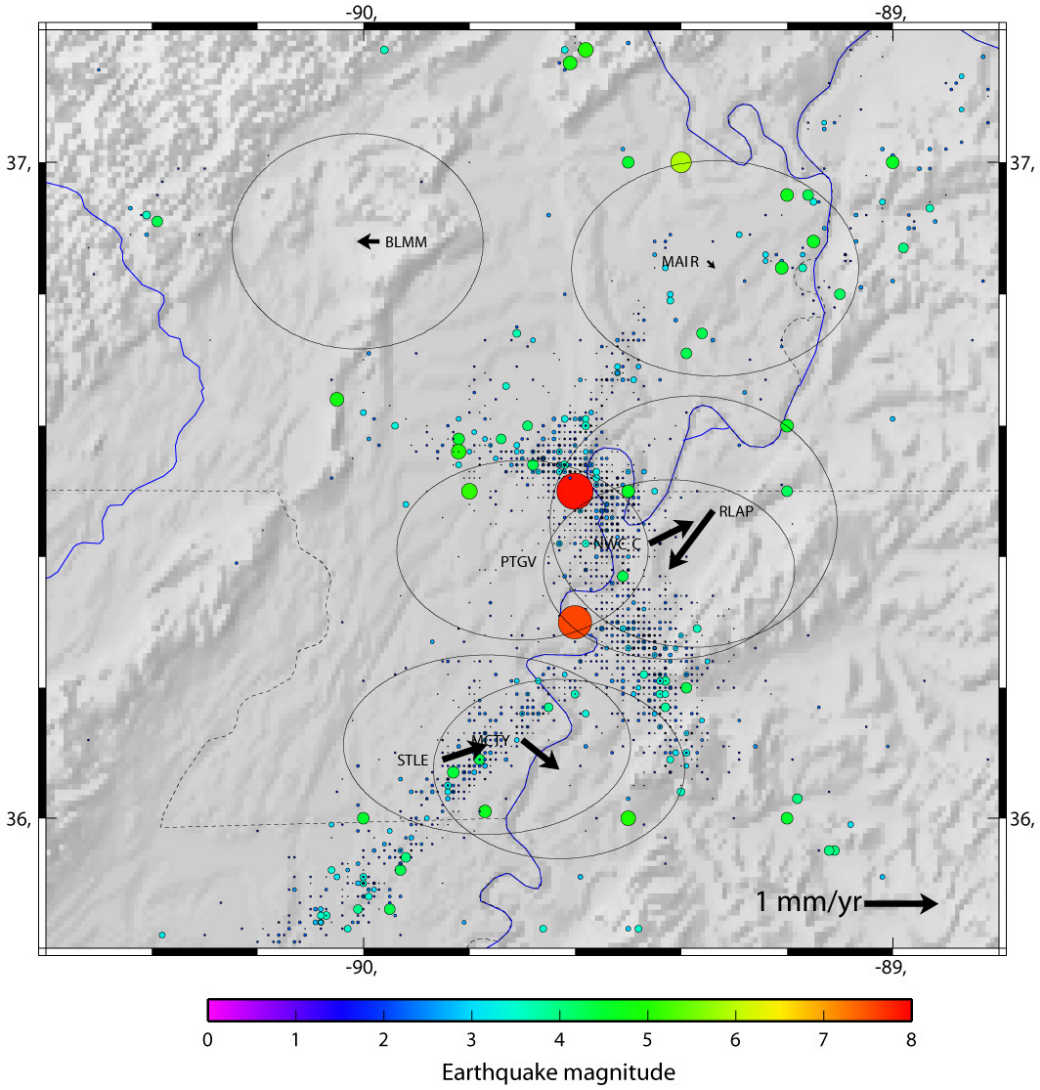

Figure 4.3: Residual velocities in the NMSZ. Seismicity is from the CERI catalog.

More recently, Smalley et al. (2005) argue that relative motions between CGPS sites in the NMSZ are significant and comparable to deformation rates along active plate boundaries.

Our results show no detectable residual motion in the NMSZ at the 95% confidence level (Figure 4.3). The average weighted residual for sites in the region with respect to the predictions of our best-fitting North American plate angular velocity vector is 0.7 mm/yr, comparable to that for sites outside the region. None of the individual site velocities are significant at the 95% confidence level.

A key question is whether the apparent shortening of 1.6±1.2 mm/yr (68% confidence) between sites RLAP and NWCC across the Reelfoot fault is significant, as recently proposed by Smalley et al. (2005). An examination of the baseline time series between these two sites (Figure 4.4) suggests that the apparent shortening is not caused by a linear decrease in the inter-station distance, as might be expected if the cause of the shortening was tectonic, but is instead a result

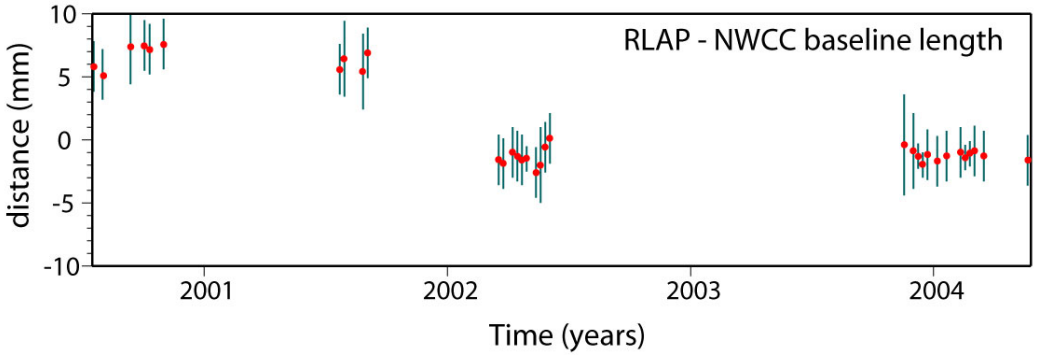

Figure 4.4: NWCC-RLAP baseline length time series (weekly solutions).

of an 8 mm offset between 2001 and 2002 that separates two periods of no discernible change in the baseline length. The offset, which originated at site NWCC, does not correspond to any equipment changes, significant earthquakes, or known creep events at or near site NWCC and is thus difficult to explain. Whatever the explanation, the apparent shortening between RLAP and NWCC reported here as well as by Smalley et al. (2005) results from this unexplained offset and is unlikely to represent steady, long-term strain accumulation on the intervening Reelfoot fault.

4.3 Implications for earthquake recurrence

Based on our 0.7 mm/yr weighted RMS value for the residual velocities of the NMSZ sites, random deviations from a rigid plate model in the NMSZ region do not exceed 1.4 mm/yr at the 95% confidence level. We assume that this represents a conservative upper bound on the magnitude of any long-term slip in the study area. Assuming a simple model where characteristic earthquakes repeat regularly on a given active fault – as is implicit in the U.S. earthquake hazard maps, for instance – our results imply a minimum repeat time of about 3,000 to 8,000 years for future magnitude 8 earthquakes with 5-10 m of coseismic slip (Figure 4.5). For comparison, National Seismic Hazard Maps assume a 1,000 year recurrence time for M8 events with 5 m of coseismic slip. The implied ∼5 mm/yr of long term slip rate on the New Madrid faults is a factor of four faster than the upper bound suggested by our analysis.

Similarly, our 1.4 mm/yr upper bound implies a minimum repeat time of 600-1,500 years for future magnitude 7 earthquakes with 1-2 m of coseismic slip (Figure 4.5). This is consistent with recent and historic earthquake catalogs, which predict a recurrence intervals exceeding 1000 years for magnitude 7 earthquakes and 10,000 years for magnitude 8 earthquakes (Newman et al., 1999). It is also consistent with paleoseismic data (Tuttle and Schweig, 1999; Kelson et al., 1996; Tuttle et al., 1999), which imply recurrence intervals of 400 to 1,000 years.

5 Conclusions

Our analysis of data from more than 300 continuous GPS sites in the North American plate interior shows that deformation north of 40N is dominated by the effects of GIA, with residual velocities up to ∼1.4 mm/yr directed south to southeast. South of that latitude, residual velocities with respect to a rigid plate model show a random pattern, with a weighted misfit of 0.7 mm/yr and no evidence for regions of elevated strain rates. In particular, we find no detectable residual

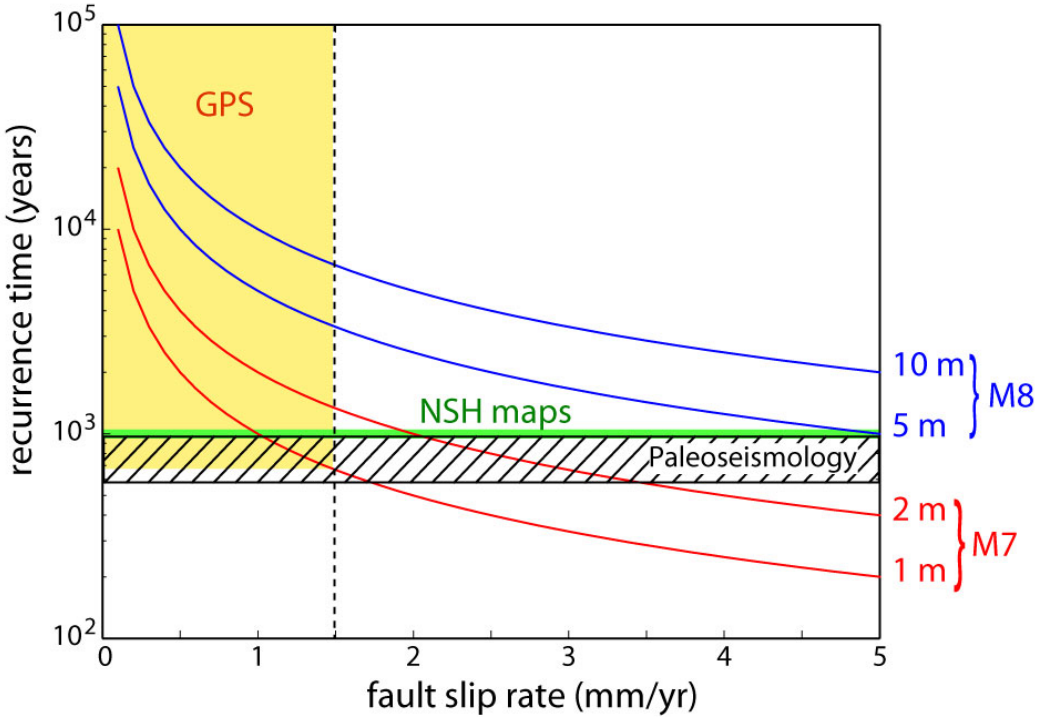

Figure 4.5: Recurrence time for M7 and M8 earthquakes, with two end-member values of coseismic slip for each magnitude (after Newman et al., 1999). NSH = National Seismic Hazard maps. Paleoseismology is from Tuttle and Schweig (1995).

motion at the 95% confidence level in the New Madrid Seismic Zone, with an average weighted misfit of 0.7 mm/yr to a rigid plate model.

These results compare well with other plate interiors. In Western Europe, magnitude 7 paleoearthquakes are inferred in the Rhine graben, but no surface deformation has yet been resolved with GPS at the 0.8 mm/yr level (Nocquet et al., 2004). In Australia, despite several significant earthquakes in the past two decades, GPS measurements show no deformation within their resolution (0.8 mm/yr, Beavan et al., 2002). Although intraplate earthquakes indicate that tectonic stresses within plate interiors accumulate on faults and are released during large infrequent events, geodetic observations on several major plates do not reflect this cycle, at least not on a time scale of a decade or less. Except for areas affected by GIA, deviations from rigid behavior within plate interiors are below the current resolution of GPS measurements. Longer observation spans and further improvement of geodetic techniques may allow us to understand where, why, and how much strain concentrates in plate interiors.

Acknowledgments. This work was supported by the U.S. Geological Survey (USGS), Department of the Interior, under USGS award number 03HQGR0001 We thank the NGS for making the CORS data publicly available, CERI for making the GAMA data publicly available, the agencies participating in the IGS, from the data collection to the realization of combined solutions, and the IERS for maintaining a high-accuracy reference frame critical for geophysical applications.

Bibliography

[1] Argus, D. F., and R. G. Gordon, Tests of the rigid-plate hypothesis and bounds on intraplate deformation using geodetic data from Very Long Baseline Interferometry, J. Geophys. Res., 101, 13,555-13,572, 1996.

[2] Argus, D.F., W.R. Peltier, and M.W. Watkins, Glacial isostatic adjustment observed using very long baseline interferometry and satellite laser ranging geodesy, J. Geophys. Res., 104, 29077-29093, 1999.

[3] Balazs, E.I., Vertical crustal movements on the middle Atlantic coastal plain as indicated by precise leveling, Geol. Soc. of Amer., Northeastern Section Annual Meeting, Boulder, Colorado, 1974.

[4] Baljinnyam, I., Bayasgalan, A., Borisov, B.A., Cisternas, A., Dem'yanovich, M.G., Ganbaatar, L., Kochetkov, V.M., Kurushin, R.A., Molnar, P., Philip, H. and Vashchilov, Y.Y., Ruptures of Major Earthquakes and Active Deformation in Mongolia and its Surroundings. Geol. Soc. Am., Mem. 181, 62 pp., 1993.

[5] Beavan, J., P. Tregoning, M. Bevis, T. Kato, and C. Meertens, Motion and rigidity of the Pacific plate and implications for plate boundary deformation, J. Geophys. Res., 107 (B10), doi:10.1029/2001JB000282, 2002.

[6] Beavan, J., Noise properties of continuous GPS data from concrete pillar geodetic monuments in New Zealand and comparison with data from U.S. deep drilled braced monuments, J. Geophys. Res., 110, B08410, doi:10.1029/2005JB003642, 2005 .

[7] Blewitt, G., and D. Lavallee, Effect of annual signals on geodetic velocity, J. Geophys. Res., 107, 10.1029/2001JB000570, 2002.

[8] Brown, L.D., and J.E. Oliver, Vertical crustal movements from leveling data and their relation to geologic structure in the eastern United states, Reviews of Geophysics and Space Physics, 14, 13-34, 1976.

[9] Dixon, T.H., A. Mao, and S. Stein, How rigid is the stable interior of the North American plate?, Geophys. Res. Lett., 23, 3,035-3,038, 1996. Frankel, A. et al., National Seismic Hazard Maps Documentation,U.S. Geol. Surv. Open file Rep. 96-532, 1996.

[10] Fernandes R.M.S, B.A.C. Ambrosius, R. Noomen, L. Bastos, L. Combrinck, J.M. Miranda, W. Spakman, Angular velocities of Nubia and Somalia from continuous GPS data: implications on present-day relative kinematics, Earth and Planetary Science Letters, 222, 197-208, 2004.

[11] Gan, W., and W.H. Prescott, Crustal deformation rates in central and eastern U.S. inferred from GPS, Geophys. Res. Letters, 19, 3733-3736, 2001.

[12] Hough, S.E., J.G. Armbuster, L. Seeber, and J.F. Hough, On the modified Mercalli intensities and magnitudes of the 1811-1812 New Madrid earthquakes, J. Geophys. Res., 105, 23839-23864, 2000.

[13] Johnston, A.C., Seismic moment assessment of earthquakes in stable continental regions. III. New Madrid 1811-1812, Charleston 1886, and Lisbon 1755, Geophys. J. Int., 126, 314, 344, 1996.

[14] King, R. W., and Y. Bock, Documentation for the GAMIT GPS software analysis, release 10.05, Mass. Inst. of Technol. Cambridge, 2001.

[15] Kogan, M. G, G. M. Steblov, R. W. King, T. A. Herring, D. I. Frolov, S. G. Egorov, V. Y. Levin, A. Lerner-Lam, and A. Jones, Geodetic constraints on the rigidity and relative motion of Eurasia and North America, Geophys. Res. Lett., 27, 2041-2044, 2000.

[16] Langbein, J., and H. Johnson, Correlated errors in geodetic time series: Implications for time-dependent deformation, J. Geophys. Res., 102, 591603, 1997.

[17] Liu, L., M.D. Zoback, and P. Segall (1992). Rapid intraplate strain accumulation in the New Madrid seismic zone, Science, 257, 1666-1669.

[18] Mao, A., C.G.A. Harrison, and T.H. Dixon, Noise in GPS coordinate time series, J. Geophys. Res., 104, 2797-2816, 1999.

[19] Marquez-Azua, B., and C. DeMets, Crustal velocity field of Mexico from continuous GPS measurements, 1993 to June, 2001: Implications for the neotectonics of Mexico, J. Geophys. Res., 108(B9), doi: 10.1029/2002JB002241, 2003.

[20] Newman, A., S. Stein, J. Weber, J. Engeln, A. Mao, and T. Dixon, Slow deformation and lower seismic hazard at the New Madrid seismic zone, Science, 284, 1999.

[21] Nocquet, J.M., E. Calais, and B. Parsons, Geodetic Constraints on Glacial Isostatic Adjustment in Europe, Geophys. Res. Letters, v.32, L06308, doi:10.1029/2004GL022174, 2005.

[22] Nuttli, O.W. (1983). Catalog of Central United States Earthquakes Since 1800 of mb>3.0, St. Louis University, St. Louis. Mo.

[23] Peltier, W.R., VLBI baseline variations from the ICE-4G model of post-glacial rebound, Geophys. Res. Lett. , 22, 465-468, 1995. Peltier, W.R., Mantle viscosity and ice-age ice sheet topography, Science, 273, 1359-1364, 1996.

[24] Sella, G. F., T. H. Dixon and A. Mao, REVEL: A model for recent plate velocities from Space Geodesy, J. Geophys. Res., 2002.

[25] Smalley R., M.A. Ellis, J. Paul, and R.B. Van Arsdale, Space geodetic evidence for rapid strain rates in the New Madrid seismic zone of central USA, Nature, Vol. 435, doi:10.1038/nature03642, June 2005.

[26] Snay, R.A., J.F. Ni, and H.C. Neugebauer, Geodetically derived strain across the northern New Madrid Seismic Zone, U.S. Geol. Surv. Prof. Pap. 1538-F, 1994.

[27] Snay, R., and N. Weston, Future directions of the national CORS system, Proceedings of the 55th Annual Meeting of the Institute of Navigation, Cambridge, MA, 301-305, 1999.

[28] Tuttle, M.P., and E.S. Schweig, Archaelogical and pedological evidence for large prehistoric earthquakes in the New Madrid seismic zone, central United States, Geology, 23, 253-256, 1995.

[29] Tuttle, M.P., J. Collier, L.W. Wolf, and R.H. Cafferty, New evidence for a large earthquake in the New Madrid seismic zone between AD 1400 and 1670, Geology, 27, 771-774, 1999.

[30] Weber, J., S. Stein, and J. Engeln, Estimation of strain accumulation in the New Madrid seismic zone from GPS geodesy, Tectonics, 17, 250-266, 1998.

[31] Williams, S. D. P., Y. Bock, P. Fang, P. Jamason, R. Nikolaidis, L. Prawirodirdjo, M. Miller, and D. Johnson, Error analysis of continuous GPS position time series, J. Geophys. Res., 109, B03412, doi:10.1029/2003JB002741, 2004.

[32] Zhang, J., Y. Bock, H. Johnson, P. Fang, S. Williams, J. Genrich, S. Wdowinski, and J. Behr, Southern California Permanent GPS geodetic array: Error analysis of daily position estimates and sites velocities, J. Geophys. Res., 102, 18,035-18,055, 1997.

[33] Zumberge, J. F., M. B. Heflin, D. C. Jefferson, M. M. Watkins, and F. H. Webb, Precise point positioning for the efficient and robust analysis of GPS data from large networks, J. Geophys. Res., 102, 5005-5017, 1997.

6 Appendix

Table 6.1: Velocities (V, mm.yr^{-1}) with respect to North America and associated one standard deviation formal errors (σ, mm.yr^{-1}).

Site	lon	lat	V_e	V_n	σ_e	σ_n	Corr.	RWN	span
ABQ1	-106.49	34.96	-1.03	-0.18	0.96	0.81	-0.0011	4.409	2.47
ACU1	-70.88	41.74	-1.12	-4.59	0.96	0.90	-0.0026	2.545	3.10
ADKS	-95.58	29.79	-1.82	-4.95	1.93	2.22	-0.0002	3.942	3.14
ADRI	-84.02	41.92	0.42	-1.20	0.77	0.63	-0.0017	0.907	3.14
ALGO	-78.07	45.95	0.32	-1.01	0.49	0.33	-0.0176	0.471	10.29
AMC2	-104.52	38.80	-0.82	0.51	0.70	0.45	0.0029	1.121	6.48
AML5	-101.88	35.15	0.10	0.02	0.75	0.54	-0.0009	0.237	6.98
ANP1	-76.61	39.01	0.69	-0.23	1.22	1.10	-0.0007	0.988	3.81
ANTO	-98.57	29.49	0.12	0.02	0.79	0.55	-0.0038	0.480	6.96
AOML	-80.16	25.73	1.36	1.80	0.72	0.48	0.0064	1.508	6.34
ARL5	-97.06	32.76	-1.11	0.68	0.76	0.49	-0.0018	0.677	6.98
ARP3	-97.06	27.84	-4.56	-0.49	0.82	0.58	-0.0036	1.663	9.26
ASHV	-82.54	35.60	-0.09	0.37	0.66	0.47	0.0000	0.500	6.71
ASUB	-81.68	36.21	0.05	0.60	1.08	0.81	-0.0001	2.799	2.26
ATL1	-84.52	33.93	-1.13	-0.18	2.07	2.82	0.0000	2.623	4.31
AUS5	-97.75	30.31	2.01	-1.70	0.85	0.67	-0.0023	7.341	6.98
BARH	-68.22	44.39	0.29	-0.26	0.57	0.52	-0.0122	0.968	6.54
BARN	-71.16	44.10	0.21	-0.88	0.71	0.64	-0.0072	1.412	4.73
BAYR	-83.89	43.44	0.28	-1.07	0.72	0.59	-0.0024	1.092	3.58
BEA5	-94.18	30.16	4.35	6.05	0.92	0.91	-0.0009	7.130	6.96
BLKV	-80.41	37.20	0.11	0.67	0.67	0.51	-0.0010	0.802	5.96
BLMM	-89.97	36.88	-0.30	0.03	0.72	0.63	0.0001	0.758	5.81
BLRW	-90.53	43.23	-0.83	0.27	0.67	0.59	0.0008	1.314	5.52
BRIG	-83.75	42.52	0.18	-0.21	0.73	0.58	-0.0022	0.987	3.58
BRMU	-64.69	32.37	0.46	0.36	0.61	0.43	0.0125	0.285	10.29
BRU1	-69.94	43.89	0.62	-0.49	0.57	0.44	-0.0130	0.226	9.26
BSMK	-100.81	46.82	0.31	0.46	0.98	0.66	0.0051	1.748	3.28
BVHS	-89.40	29.34	-2.59	-1.87	1.00	0.86	-0.0001	2.797	2.28
CAGS	-75.80	45.58	0.30	-0.97	0.67	0.62	-0.0076	1.360	3.28
CASL	-77.87	34.34	0.42	-0.93	1.44	1.53	0.0002	2.481	3.01
CCV1	-80.54	28.46	-1.22	-0.82	2.78	3.33	0.0002	2.369	2.47
CCV3	-80.54	28.46	-0.67	-0.10	0.87	0.85	0.0021	1.095	6.69
CHA1	-79.84	32.76	0.52	0.04	0.69	0.54	0.0019	0.884	7.82
CHB1	-84.46	45.65	0.43	-0.16	0.58	0.42	-0.0048	0.463	9.26
CHL1	-75.09	38.78	-0.35	-0.71	0.69	0.53	-0.0025	0.743	5.94
CHME	-80.89	35.28	0.14	1.14	0.84	0.70	0.0001	1.706	3.18
CHR1	-76.00	36.93	-0.44	-4.25	1.52	1.58	-0.0001	0.898	3.41
CHT1	-69.95	41.67	-0.70	-0.42	0.81	0.85	-0.0033	0.461	6.38
CHUR	-94.09	58.76	0.88	-0.75	0.48	0.41	0.0158	0.869	8.82
CJTR	-92.27	34.82	0.16	-0.18	0.75	0.57	-0.0002	0.688	5.54
CLK1	-97.96	44.93	0.61	-1.80	0.77	0.69	0.0040	1.914	5.75

CNWM	-92.70	37.52	-0.24	0.02	0.73	0.56	0.0005	0.555	6.00
COGA	-82.13	33.54	-0.57	1.21	0.82	0.70	0.0006	1.305	3.18
COLA	-81.12	34.08	0.78	0.98	0.68	0.56	0.0008	1.874	6.29
COLB	-83.04	39.96	-0.58	-0.52	0.74	0.58	-0.0016	1.216	3.33
CONO	-81.23	35.70	-0.20	0.69	0.89	0.76	0.0000	1.427	3.55
CORB	-77.37	38.20	-0.32	-0.32	0.71	0.65	-0.0014	0.607	4.14
CORC	-97.44	27.74	-0.24	0.86	0.80	0.56	-0.0041	1.084	6.98
DEFI	-84.41	41.28	-0.93	0.50	0.78	0.60	-0.0014	1.106	3.33
DET1	-83.09	42.30	0.19	-0.81	0.62	0.45	-0.0036	1.246	9.26
DFNK	-86.15	30.73	0.54	-0.48	0.93	0.70	0.0005	2.935	2.89
DNRC	-75.52	39.16	-0.04	-0.44	0.61	0.48	-0.0035	0.965	7.05
DQUA	-94.29	34.11	0.20	0.58	0.71	0.45	-0.0007	0.331	8.28
DRV1	-76.55	36.96	0.52	1.42	0.76	0.63	-0.0006	0.867	5.75
DUBO	-95.86	50.26	-0.31	-1.09	0.64	0.51	0.0082	0.335	8.49
DUCK	-75.75	36.18	-0.40	0.90	0.70	0.59	0.0000	14.825	6.46
EKY1	-82.76	27.60	-2.66	0.38	1.35	1.89	0.0005	66.520	5.31
ENG1	-89.94	29.88	-0.85	0.73	0.79	0.59	-0.0004	1.116	9.26
EPRT	-66.99	44.91	1.13	-0.28	0.56	0.51	-0.0141	0.660	6.54
ERLA	-84.60	39.02	0.32	0.05	0.61	0.40	-0.0016	0.390	8.45
FAYR	-78.87	35.03	0.30	0.99	0.82	0.75	0.0003	1.488	3.99
FBYN	-97.31	40.08	-0.22	0.44	0.70	0.53	0.0025	0.691	6.00
FDTC	-79.81	34.24	7.84	-4.61	1.21	1.31	0.0002	10.314	3.83
FLIN	-101.97	54.72	0.33	-1.41	0.56	0.44	0.0252	0.481	8.85
FMC2	-76.68	34.70	-4.54	1.40	1.86	2.22	0.0001	5.648	4.02
FREO	-81.26	40.20	0.77	-0.61	1.27	1.11	-0.0006	1.248	3.12
GAL1	-94.73	29.33	0.31	-0.75	0.79	0.54	-0.0023	0.530	7.47
GALB	-84.48	39.21	0.69	-0.01	0.63	0.43	-0.0016	0.539	7.28
GALP	-82.28	38.84	0.57	-0.54	0.89	0.72	-0.0009	2.003	2.28
GAST	-81.19	35.31	-6.84	-1.78	2.37	2.61	0.0000	12.673	2.15
GDAC	-102.18	37.77	-0.15	0.67	0.71	0.45	0.0016	0.333	8.49
GDMA	-90.34	47.75	0.12	-1.33	0.81	0.70	0.0008	1.584	2.89
GLPT	-76.50	37.25	0.26	0.28	0.64	0.52	-0.0011	0.913	5.42
GNVL	-82.27	29.69	0.31	-1.13	0.95	0.75	0.0014	2.495	2.89
GODE	-76.82	39.02	0.14	0.00	0.55	0.34	-0.0050	0.285	10.29
GRAR	-85.67	42.99	0.04	-0.81	0.73	0.66	-0.0013	1.656	3.58
GUST	-80.71	41.46	0.09	-0.80	0.77	0.63	-0.0025	1.311	3.12
GVLT	-82.37	34.83	1.49	-0.84	0.85	0.88	0.0002	1.519	3.83
HAG2	-77.71	39.55	0.66	0.25	1.57	1.47	-0.0005	1.316	3.76
HAMM	-90.46	30.51	-0.89	-0.21	0.92	0.71	-0.0004	2.069	3.22
HAMP	-72.64	42.32	1.37	-2.81	0.85	1.21	-0.0023	4.131	2.47
HAYW	-82.92	35.53	0.86	1.65	0.90	0.80	0.0000	1.829	2.47
HBRK	-97.29	38.30	0.25	-0.45	0.67	0.42	0.0019	0.871	9.98
HCES	-89.17	36.33	-3.55	0.98	0.83	1.01	0.0000	3.190	4.66
HDF1	-73.54	43.27	-4.72	-11.76	0.89	0.87	-0.0034	19.269	4.41
HILB	-79.10	36.05	0.06	-0.02	1.03	0.73	-0.0001	2.242	3.01
HIPT	-80.01	35.96	-0.45	0.95	0.71	0.56	-0.0001	1.726	5.17
HKLO	-95.86	35.68	-0.39	-0.36	0.69	0.42	-0.0001	0.393	9.97

HLFX	-63.61	44.68	0.43	-0.28	0.89	0.90	-0.0049	1.915	2.30
HNPT	-76.13	38.59	-0.09	-0.63	0.64	0.47	-0.0027	2.526	5.42
HOUS	-95.43	29.78	-2.35	0.19	0.85	0.65	-0.0019	0.803	6.96
HRN1	-78.18	40.88	0.57	-1.14	0.87	0.98	-0.0016	7.816	3.55
HVLK	-99.10	37.65	-1.07	-0.07	0.69	0.45	0.0015	6.301	8.85
IUCO	-86.50	39.17	0.59	1.12	0.69	0.53	-0.0007	1.111	4.94
JTNT	-100.97	33.02	-0.29	-0.14	0.75	0.47	-0.0028	0.646	7.90
JXVL	-81.70	30.48	0.39	-0.91	1.01	0.81	0.0012	3.555	2.89
KJUN	-92.04	30.22	-0.12	-3.91	1.07	1.48	-0.0003	46.533	3.22
KNTN	-83.61	40.63	0.00	-0.29	0.86	0.72	-0.0011	3.199	2.28
LAMT	-73.91	41.00	-1.09	-0.82	0.70	0.67	-0.0038	1.100	3.66
LANS	-84.66	42.67	0.03	-1.29	0.77	0.60	-0.0017	1.168	3.01
LCDT	-87.96	42.29	0.50	-0.53	0.76	0.63	-0.0004	0.769	3.53
LEBA	-84.28	39.43	0.19	-0.55	0.75	0.57	-0.0011	0.989	3.33
LKHU	-95.14	29.91	0.48	2.22	0.77	0.51	-0.0025	0.960	9.60
LOU1	-85.30	38.01	-0.60	1.88	0.81	0.74	-0.0004	2.020	7.21
LSBN	-80.81	40.77	-0.30	-0.56	0.88	0.70	-0.0017	1.801	2.28
LTHM	-94.17	39.57	-0.23	-0.17	0.72	0.56	0.0013	0.555	6.00
LUBB	-101.84	33.53	-0.45	-0.34	0.78	0.56	-0.0021	0.294	6.98
LYCO	-77.00	41.24	0.79	0.01	1.72	1.63	-0.0006	1.373	2.80
MACC	-90.48	37.84	0.15	0.08	0.73	0.49	0.0002	0.745	5.50
MAIR	-89.35	36.85	0.09	-0.13	0.77	0.62	0.0000	1.151	5.12
MARI	-81.95	35.65	-0.08	-0.34	0.89	0.85	0.0000	2.128	2.45
MCD1	-82.53	27.85	0.94	-1.22	0.86	0.71	0.0021	2.868	3.95
MCN1	-83.56	32.69	-0.31	0.20	0.74	0.58	0.0009	1.170	5.06
MCNE	-93.21	30.18	-0.59	-2.05	1.71	1.53	-0.0002	8.405	2.28
MCON	-81.83	39.66	0.11	-0.31	0.75	0.59	-0.0017	1.011	3.32
MCTY	-89.70	36.12	0.52	-0.40	0.72	0.52	0.0000	1.532	4.98
MDO1	-104.01	30.68	-0.36	-0.08	0.75	0.39	-0.0077	0.685	10.29
MEM2	-90.20	35.46	-1.82	0.07	0.72	0.47	-0.0001	1.245	9.26
METR	-83.24	42.68	0.45	-0.90	0.73	0.58	-0.0025	0.854	3.58
MIA1	-80.16	25.73	-1.49	-0.20	2.87	3.48	0.0002	3.471	2.38
MIA3	-80.16	25.73	0.82	0.40	0.79	0.60	0.0048	1.320	6.86
MIL1	-87.89	43.00	0.02	0.26	0.61	0.43	-0.0008	0.491	9.26
MIO1	-84.13	44.65	-0.77	-1.05	2.16	2.19	-0.0002	2.986	2.36
MLF1	-87.39	32.09	-0.46	1.46	0.71	0.52	0.0003	1.540	8.53
MNP1	-71.86	41.07	-1.66	0.35	2.08	2.04	-0.0004	1.808	2.70
MOB1	-88.02	30.23	-1.37	-0.43	0.74	0.50	0.0003	0.491	9.01
MOR1	-72.74	40.79	-0.19	-0.46	0.61	0.49	-0.0058	0.791	6.52
MPLE	-84.76	43.61	0.27	-0.48	0.82	0.71	-0.0015	1.186	3.18
MRRN	-101.69	42.90	-0.61	0.82	0.70	0.53	0.0060	1.294	6.21
MTVR	-82.51	40.38	0.07	-0.81	0.85	0.71	-0.0013	2.030	2.28
NBR2	-77.05	35.17	-0.07	-0.94	0.75	0.69	0.0005	1.379	4.31
NDBC	-89.61	30.36	-0.73	0.38	0.73	0.47	-0.0004	3.459	8.47
NDS1	-95.60	37.30	-0.40	0.82	0.84	0.66	0.0005	0.911	4.18
NDSK	-95.64	37.38	0.15	-0.08	0.84	0.61	0.0006	1.040	3.95
NEB3	-84.15	46.32	1.50	2.08	1.40	1.10	-0.0009	2.593	3.64

NETP	-95.33	29.79	1.88	-2.51	1.62	1.77	-0.0004	3.002	3.10
NJI2	-74.18	40.74	0.14	0.26	1.14	1.18	-0.0012	2.156	3.91
NLIB	-91.57	41.77	0.16	0.19	0.58	0.35	0.0021	0.646	10.29
NMSF	-105.96	35.67	1.03	-1.06	2.36	2.82	-0.0001	3.308	2.22
NOR1	-85.43	44.25	0.57	-1.12	0.73	0.59	-0.0018	1.040	3.58
NOR2	-84.68	44.99	0.53	-0.80	0.71	0.61	-0.0024	1.066	3.58
NOR3	-83.57	45.07	-0.11	-1.61	0.72	0.62	-0.0029	1.092	3.58
NRC1	-75.62	45.45	0.30	-0.65	0.51	0.37	-0.0170	0.737	9.12
NWCC	-89.46	36.42	0.55	0.31	0.83	0.72	0.0000	2.841	4.08
ODS5	-102.31	31.87	0.12	-1.02	0.79	0.58	-0.0033	0.357	6.98
OKAD	-96.74	34.80	-0.69	-0.89	2.56	3.52	0.0000	2.658	2.47
OKAN	-95.62	34.19	0.10	-0.59	0.90	0.80	-0.0004	2.552	2.66
OKCB	-80.85	27.27	-0.40	-1.12	0.99	1.02	0.0017	3.172	2.36
OKCL	-98.97	35.48	0.39	-1.38	1.03	0.94	-0.0001	3.499	2.32
OKDT	-97.50	35.49	0.75	0.43	0.99	0.86	-0.0001	2.656	2.87
OKEE	-82.59	42.91	-0.12	-1.80	1.43	1.28	-0.0007	1.574	2.80
OKLW	-98.41	34.57	1.31	-0.82	1.08	0.93	-0.0003	6.013	2.47
OKMU	-95.40	35.72	0.60	1.26	1.02	1.21	0.0000	8.691	2.66
OKOM	-88.86	34.09	-0.30	-0.27	0.94	1.04	0.0000	0.722	5.27
OKTE	-96.89	35.26	-0.07	-0.86	0.88	0.81	-0.0002	3.036	2.66
OKTU	-95.85	36.21	-1.93	-0.22	0.97	1.46	0.0001	6.428	2.47
OSPA	-76.51	43.46	-0.72	-1.18	0.89	0.70	-0.0038	2.795	2.93
PATT	-95.72	31.78	-0.15	-0.15	0.76	0.50	-0.0019	0.292	7.90
PIE1	-108.12	34.30	-0.04	-0.70	0.76	0.45	-0.0039	1.862	10.29
PIGT	-90.17	36.37	-3.89	-6.67	0.95	0.90	0.0000	24.394	5.04
PIT1	-79.69	40.55	0.42	-0.36	0.60	0.41	-0.0046	0.641	8.16
PKTN	-83.02	39.04	0.37	-0.82	0.73	0.59	-0.0012	0.938	3.32
PLTC	-104.72	40.18	-0.47	-0.11	0.69	0.44	0.0048	0.599	10.23
PLTK	-81.69	29.66	-0.02	-1.00	0.93	0.77	0.0015	2.786	2.89
PNB1	-68.77	44.45	1.55	0.05	0.60	0.56	-0.0108	0.846	6.02
PNCY	-85.68	30.20	-0.17	-0.53	0.99	0.76	0.0006	4.431	2.89
PNR1	-94.72	46.86	-1.02	2.14	1.59	1.73	0.0006	1.453	3.16
PRCO	-97.52	34.98	-0.17	-0.08	0.70	0.42	-0.0007	0.424	9.37
PSC1	-74.25	44.43	0.02	-0.92	0.66	0.59	-0.0078	0.981	4.08
PSU1	-77.85	40.81	0.03	0.08	0.60	0.42	-0.0056	0.715	7.49
PTGV	-89.70	36.41	0.03	0.04	0.71	0.51	0.0000	0.731	6.09
PUB1	-104.34	38.29	-0.03	-1.41	1.41	1.32	0.0004	2.368	3.43
RALR	-78.64	35.79	-1.06	0.22	0.77	0.82	0.0000	9.604	4.04
RCM5	-80.38	25.61	0.31	-0.59	0.80	0.50	0.0056	4.890	1.76
RCM6	-80.38	25.61	0.31	-0.59	0.80	0.51	0.0055	6.929	1.88
RED1	-75.57	39.56	0.44	0.02	0.68	0.59	-0.0029	1.199	6.19
RESO	-94.89	74.69	-1.25	-1.58	1.15	1.12	0.0045	14.758	3.28
RIS1	-90.22	42.01	-0.68	1.88	0.73	0.64	0.0005	0.947	8.39
RLAP	-89.34	36.47	-0.58	-0.80	0.71	0.51	0.0000	0.812	7.00
RWDN	-100.65	40.09	-0.67	-0.02	0.73	0.53	0.0032	0.702	6.00
SAG1	-83.84	43.63	-2.40	-0.85	0.59	0.42	-0.0043	0.646	9.26
SAV1	-81.69	32.14	0.01	0.34	0.72	0.53	0.0017	1.115	6.36

SCH2	-66.83	54.83	0.03	0.15	0.47	0.44	-0.0442	0.935	7.63
SCUB	-75.76	20.01	2.81	-1.35	1.01	0.74	0.0072	9.662	1.72
SG00	-97.08	47.92	0.19	0.48	2.42	3.15	0.0003	2.344	2.53
SG01	-97.48	36.60	0.38	0.53	0.82	0.64	0.0003	1.145	3.76
SG04	-97.26	37.13	0.80	0.71	0.79	0.61	0.0006	1.095	3.58
SG05	-80.62	28.06	-0.33	-3.28	1.78	2.82	0.0003	2.120	3.20
SG06	-73.12	40.91	-1.27	-0.56	1.06	1.18	-0.0014	1.740	2.70
SG07	-68.67	44.90	-0.12	-0.14	0.78	1.08	-0.0046	1.408	3.47
SG08	-96.42	36.84	0.69	0.33	0.79	0.62	0.0004	1.115	3.56
SG09	-98.28	36.43	0.68	0.28	0.84	0.72	0.0002	1.092	3.58
SG10	-98.28	36.88	0.62	0.12	0.82	0.61	0.0005	1.115	3.56
SG11	-99.31	37.33	0.29	0.21	0.79	0.64	0.0007	1.415	3.45
SG12	-99.31	38.20	1.25	0.65	0.85	0.71	0.0010	1.287	3.45
SG13	-97.51	38.11	1.15	-0.12	0.82	0.66	0.0009	1.470	3.49
SG14	-97.02	37.84	1.26	0.66	0.83	0.64	0.0008	1.113	3.47
SG15	-95.59	38.20	0.64	0.32	0.81	0.68	0.0008	1.416	3.41
SG16	-96.18	37.38	1.03	0.05	0.80	0.59	0.0006	1.108	3.41
SG18	-98.20	34.88	0.73	0.25	0.87	0.72	-0.0004	0.916	3.51
SG19	-98.97	35.35	0.58	0.27	0.82	0.63	-0.0003	1.014	3.51
SG20	-98.01	35.56	1.21	-3.00	0.82	0.61	-0.0002	1.173	3.55
SHK1	-74.01	40.47	3.83	0.82	0.60	0.44	-0.0059	1.252	9.26
SIBY	-83.24	42.17	0.54	-1.00	0.77	0.72	-0.0018	1.394	2.86
SIDN	-84.17	40.31	-0.13	-0.97	0.73	0.56	-0.0015	1.072	3.33
SLAI	-93.70	41.90	1.32	-0.10	0.70	0.55	0.0021	0.961	5.52
SNFD	-79.16	35.47	-0.73	0.21	0.88	0.76	0.0001	1.742	2.99
SOL1	-76.45	38.32	-0.02	-0.07	0.59	0.44	-0.0028	0.864	5.42
SOWR	-85.53	42.22	0.96	-2.13	0.80	0.62	-0.0012	2.967	3.56
STB1	-87.31	44.79	-0.26	-0.13	0.64	0.49	-0.0012	0.379	9.24
STKR	-82.10	39.32	-0.18	0.02	0.69	0.56	-0.0017	1.222	5.14
STL3	-89.76	38.61	-0.64	0.49	0.66	0.47	0.0002	0.544	8.87
STL4	-89.76	38.61	1.19	-0.67	0.76	0.85	0.0001	12.187	6.15
STLE	-89.85	36.09	0.58	0.18	0.76	0.52	0.0000	1.569	4.89
STP1	-91.90	44.30	-0.18	0.48	0.64	0.47	0.0023	0.568	8.66
SUM1	-102.51	34.82	-0.49	-1.35	0.87	0.68	-0.0009	1.918	4.22
SUP1	-88.44	46.75	-0.25	0.76	0.76	0.63	-0.0003	1.532	3.56
SUP2	-87.07	45.75	0.70	-1.47	0.72	0.60	-0.0011	1.057	3.56
SUP3	-85.51	46.30	0.48	-2.96	0.70	0.65	-0.0021	1.381	3.56
SYCN	-76.09	43.11	-0.98	-0.52	0.62	0.58	-0.0063	0.857	5.52
TALH	-84.35	30.40	-0.25	-0.25	0.97	0.86	0.0007	2.510	2.89
TCUN	-103.61	35.08	-0.55	0.09	0.75	0.50	-0.0014	0.722	7.32
THU1	-68.79	76.53	-1.40	-1.27	0.74	0.79	-0.0313	1.022	7.59
TIFF	-83.15	41.07	0.42	-0.39	0.76	0.59	-0.0018	1.147	3.33
TLDO	-83.47	41.61	-0.58	-0.47	0.83	0.74	-0.0014	1.812	2.28
UIUC	-88.22	40.10	-0.30	0.89	0.87	0.90	-0.0001	1.232	3.14
UNIV	-84.38	42.28	0.70	-0.89	0.73	0.59	-0.0019	0.897	3.56
UPTC	-79.66	41.63	-0.76	-0.45	0.69	0.64	-0.0032	0.688	4.56
USNO	-77.06	38.92	0.09	0.03	0.55	0.34	-0.0048	0.432	7.95

VCAP	-72.58	44.26	0.49	-0.56	0.55	0.41	-0.0143	0.457	8.62
VCIO	-99.21	36.07	0.62	1.67	0.70	0.43	0.0001	2.084	9.98
VIC1	-90.92	32.33	0.78	-2.13	0.72	0.47	-0.0006	1.149	9.26
VIMS	-75.68	37.61	-0.10	0.41	0.64	0.47	-0.0016	1.875	5.42
WASR	-77.06	35.56	-0.34	1.44	0.83	0.71	0.0002	1.436	4.06
WDLM	-95.45	44.67	-0.78	-0.10	0.70	0.55	0.0040	1.316	5.52
WES2	-71.49	42.61	-0.10	-0.72	0.51	0.32	-0.0159	1.878	10.29
WHN1	-103.33	42.74	-0.44	0.19	0.72	0.54	0.0061	0.571	6.46
WHP1	-84.96	46.77	-0.21	-2.01	0.85	0.63	-0.0021	0.808	3.68
WIL1	-76.01	41.30	-0.03	-0.31	0.56	0.38	-0.0081	0.608	8.16
WIS1	-92.01	46.70	-0.39	-0.41	0.61	0.45	0.0034	0.487	9.01
WLCI	-87.05	40.81	-0.67	-0.37	0.65	0.52	-0.0008	1.273	6.40
WNCI	-90.47	39.66	-1.92	0.96	0.77	0.61	0.0004	1.778	4.87
WNFL	-92.78	31.90	0.02	-0.73	0.76	0.51	-0.0010	0.431	7.90
WOOS	-81.96	40.80	0.03	-0.81	0.74	0.58	-0.0022	0.995	3.33
YORK	-76.74	39.99	-0.01	-0.19	0.87	0.88	-0.0016	2.362	2.28
YOU1	-78.97	43.23	0.41	-0.98	0.63	0.52	-0.0057	0.639	9.01
ZMP1	-93.15	44.64	0.70	-0.62	0.94	0.95	0.0011	5.729	2.34